

## Tornadogenesis in the 12 May 2010 Supercell Thunderstorm Intercepted by VORTEX2 near Clinton, Oklahoma

PAUL M. MARKOWSKI, TIMOTHY P. HATLEE, AND YVETTE P. RICHARDSON

*Department of Meteorology and Atmospheric Science, The Pennsylvania State University, University Park, Pennsylvania*

(Manuscript received 31 May 2018, in final form 4 September 2018)

### ABSTRACT

The 12 May 2010 supercell thunderstorm intercepted by the Second Verification of the Origins of Rotation in Tornadoes Experiment (VORTEX2) is analyzed during a time period of strong low-level rotation in which dual-Doppler radar observations were collected. Two different cyclonic vortices are documented. The first vortex was “marginally tornadic” before abruptly weakening, following the development of a descending reflectivity core (DRC) similar to those that have been documented in past studies of supercells. The second vortex rapidly developed immediately north of the DRC shortly after the DRC reached low altitudes, and was associated with a tornado that produced damage near Clinton, Oklahoma. The paper explores the possible roles of the first vortex in triggering the DRC, the DRC in the subsequent initiation of a new updraft pulse on its flank, and the updraft pulse on the development of the second, stronger vortex. The Clinton storm case is, unfortunately, a nice example of the challenges in predicting tornadogenesis within supercell storms even in environments understood to be favorable for tornadoes.

### 1. Introduction

#### *a. A brief summary of the current state of supercell and tornado prediction*

In the words of [Davies-Jones \(2015, p. 274\)](#), “Supercells are well-organized, monolithic units of vigorous long-lasting convection. A classic supercell in its mature stage consists of a rotating updraft (mid-altitude mesocyclone) and a downdraft that coexists symbiotically with the updraft in an almost steady state.” Much is known about the development of vertical vorticity within supercells, both at midlevels and near the ground (the latter is usually delayed until the storm matures and develops precipitation, downdrafts, and cool outflow at low levels). Extensive reviews have been written by [Davies-Jones et al. \(2001\)](#), [Markowski and Richardson \(2009, 2014\)](#), and [Davies-Jones \(2015\)](#).

Forecasters and convection-allowing models now routinely (and accurately) identify environments that can support supercells, and forecasters today even are relatively skillful in discriminating between

environments capable of supporting strong-to-violent (EF2+) tornadoes and environments that favor only weakly tornadic or nontornadic supercells. The vast majority (85%)<sup>1</sup> of significant tornadoes occur within tornado watches issued by the Storm Prediction Center, and major outbreaks often have lead times of 3–7 days.

Despite the advances in understanding, technology, and prediction capabilities, we still have only a limited ability to predict specific storm behavior. Even in tornado outbreaks, typically far fewer than 100% of the storms are tornadic, and those that do produce tornadoes are tornadic for only a fraction of their lifetimes despite continuously being in favorable environments. A better understanding is needed of what can trigger a storm in a favorable environment to suddenly make a tornado at a particular stage in its evolution. This was one of the motivations for the Second Verification of the Origins of Rotation in Tornadoes Experiment (VORTEX2), which was conducted in the U.S. Great Plains region in May and June of 2009 and 2010 ([Wurman et al. 2012](#)).

---

*Corresponding author:* Paul M. Markowski, [pmarkowski@psu.edu](mailto:pmarkowski@psu.edu)

---

<sup>1</sup>This figure is based on tornado reports from 2011 to 2015, courtesy of B. Smith, Storm Prediction Center.

### b. Overview of the Clinton, Oklahoma, storm

In this article, the 12 May 2010 storm from VORTEX2 is analyzed, hereafter referred to as the Clinton storm. The Clinton storm was initiated along a dryline in the southeastern Texas Panhandle shortly after 2100 UTC (Fig. 1). The storm quickly became a supercell, which was expected given the strong vertical wind shear ( $\sim 35 \text{ m s}^{-1}$  wind velocity differential over the lowest 6 km) and convective available potential energy (CAPE;  $>4000 \text{ J kg}^{-1}$  where the storm developed). VORTEX2 assets sampled the storm intermittently from 2230 to 0100 UTC as it tracked northeastward. Despite the storm's longevity and intensity, the storm was nontornadic throughout this time period (Figs. 2a–f).

The character of the storm began to change rapidly after 0100 UTC (13 May), as sunset approached and the storm neared Clinton. By this time, despite less CAPE than was present in the late afternoon immediately east of the dryline, the environment was more favorable for tornado formation (Thompson et al. 2003; Markowski et al. 2003), with strong low-level shear [ $0\text{--}1\text{-km}$  ( $0\text{--}3 \text{ km}$ ) storm-relative helicity  $\geq 200$  ( $\geq 400 \text{ m}^2 \text{ s}^{-2}$ ), high boundary layer relative humidity, and a significant tornado parameter (STP; Thompson et al. 2012) of  $2.8\text{--}4.0^2$  present on a sounding obtained near Fort Cobb, Oklahoma, approximately 65 km southeast of the Clinton storm (Fig. 3). The improvement in the environment can be attributed both to the storm's movement farther east (low-level shear and boundary layer relative humidity increased toward the east, moving away from the dryline) and the boundary layer cooling and increase in vertical shear that typically occurs in the early evening (Maddox 1993; Mead and Thompson 2011; Coffey and Parker 2015; Anderson-Frey et al. 2016).

This article focuses on the 0106–0138 UTC period, during which time dual-Doppler data were collected by the Doppler on Wheels (DOW; Wurman et al. 1997, 2001) mobile radars (Figs. 2g–i; Fig. 4). From 0106 to 0126 UTC, the storm might be referred to as “marginally tornadic,” that is, when the mesocyclone had an inbound–outbound radial velocity differential ( $\Delta v$ ) of  $30\text{--}40 \text{ m s}^{-1}$ . Alexander and Wurman (2008) used a  $40 \text{ m s}^{-1}$   $\Delta v$  threshold for identifying a vortex as a tornado; the rationale was that the corresponding rotational velocity of  $20 \text{ m s}^{-1}$ , combined with a translational

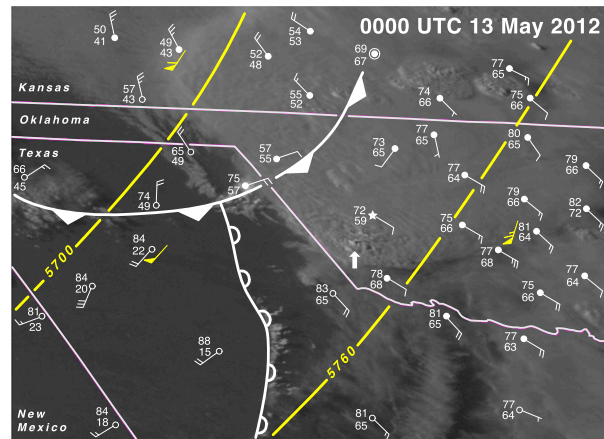


FIG. 1. Large-scale surroundings of the Clinton, OK, storm at 0000 UTC 13 May. The Clinton storm is indicated with a white arrow and the city of Clinton is indicated with a star. The visible satellite image is from *GOES-II*. Surface air mass boundaries and surface observations are overlaid in white. The station models indicate temperatures, dewpoints ( $^{\circ}\text{F}$ ), and winds (half barb =  $2.5 \text{ m s}^{-1}$ ; full barb =  $5 \text{ m s}^{-1}$ ). Cold front and dryline boundaries are indicated with filled pips and unfilled scallops, respectively. Yellow contours indicate 500-hPa geopotential heights of 5700 and 5760 m; 500-hPa wind observations also are indicated in yellow (flag =  $25 \text{ m s}^{-1}$ ).

velocity of  $\sim 10 \text{ m s}^{-1}$ , is capable of producing damage. *Storm Data* lists an EF0 tornado from 0121 to 0126 UTC, though VORTEX2 crews did not witness a funnel cloud or flying debris at any time during the marginally tornadic period. Low-level rotation rapidly intensified thereafter, and a more significant tornado produced EF1 damage on the east side of Clinton between 0126 and 0135 UTC, according to *Storm Data*.

Following a brief explanation of the available data and the analysis methods in section 2, a detailed description of the chain of events that led to tornadogenesis are presented in sections 3 and 4. The evolution of the Clinton storm was much more complicated than meets the eye, including a descending reflectivity core (DRC; Rasmussen et al. 2006; Kennedy et al. 2007a,b; Byko et al. 2009), new updraft development immediately prior to tornadogenesis, and two different cyclonic circulations during the dual-Doppler data collection period. DRCs have been identified as frequent precursors of tornadogenesis in many supercells. In the 5 June 2009 supercell intercepted by VORTEX2 (the Goshen County, Wyoming, storm), a DRC was suggested as a possible trigger of tornadogenesis (Markowski et al. 2012a,b). The Clinton storm is worth documenting because of the aforementioned importance of identifying triggers of tornadogenesis, and because the role of the DRC in tornadogenesis appears to differ

<sup>2</sup> The exact values depend on whether “fixed layer” or “effective layer” STP is considered.

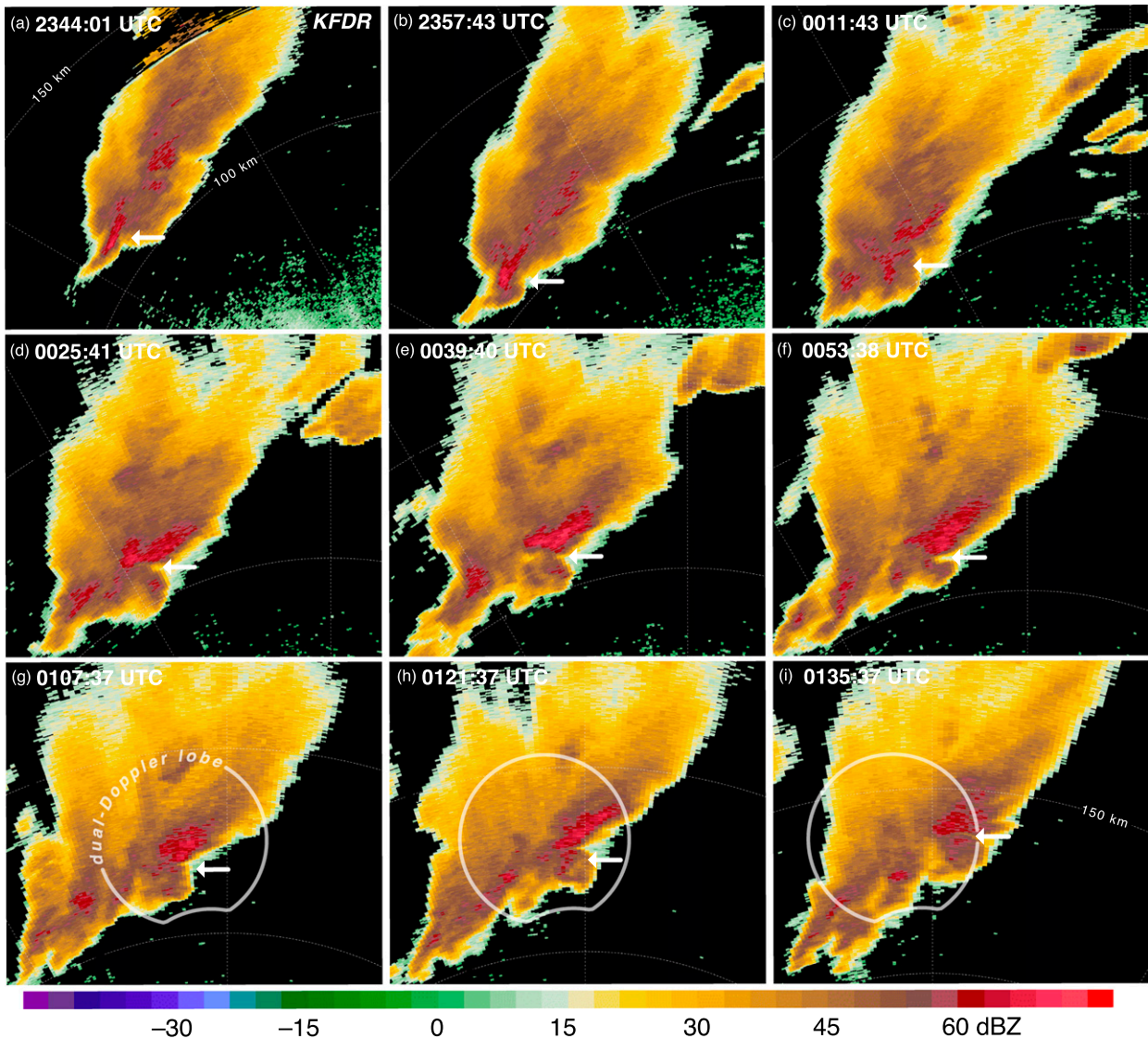


FIG. 2. Logarithmic reflectivity factor (dBZ) at the  $0.5^\circ$  elevation angle observed by the WSR-88D at Frederick, OK (KFDR), at (a) 2344, (b) 2357, (c) 0011, (d) 0025, (e) 0039, (f) 0053, (g) 0107, (h) 0121, and (i) 0135 UTC. The small arrows indicate the locations of relative maxima in azimuthal wind shear (i.e., the locations of the midlevel mesocyclone) in the storm intercepted by VORTEX2 crews. Range rings are overlaid at 50-km intervals. The dual-Doppler lobe is overlaid in (g)–(i).

from that in the Goshen County storm. [Section 5](#) contains a discussion of the findings. Last, [section 6](#) contains a summary and conclusions.

## 2. Data and analysis techniques

### a. Mobile radar data

The analysis of the Clinton storm relies principally on the dual-Doppler data collected by the DOW6 and DOW7 mobile X-band radars from 0106 to 0138 UTC ([Fig. 4](#)). The dual-Doppler lobe encloses the region in which the angle between the DOW6 and DOW7

radar beams is between  $20^\circ$  and  $160^\circ$ . The DOW6 and DOW7 radars collected volumes consisting of 11 elevation angles ( $0.5^\circ$ – $14.0^\circ$ ) every 2 min from 0103–0147 to 0105–0205 UTC, respectively. The near-surface cyclonic circulation exited the dual-Doppler lobe by approximately 0140 UTC. The DOW6 and DOW7 reflectivities are uncalibrated.

Mobile radar data also were collected by the NSSL X-band, dual-polarization radar (NOXP; [Melnikov et al. 2009](#); [Palmer et al. 2009](#)) from 0146 to 0214 UTC, from near Weatherford, Oklahoma ([Fig. 4](#)). Dual-Doppler, three-dimensional wind retrievals are not

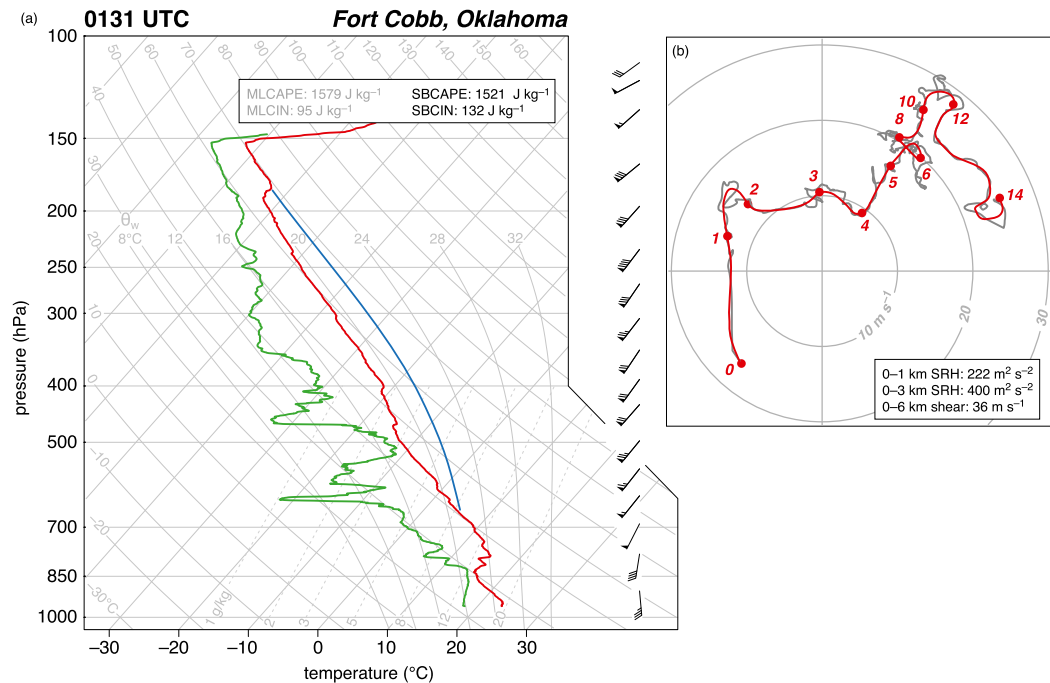


FIG. 3. (a) Skew  $T$ - $\log p$  diagram of the 0131 UTC 13 May NSSL1 sounding launched near Fort Cobb, OK, approximately 65 km southeast of the Clinton tornadic supercell. The wind barbs are ground-relative (half barb =  $2.5 \text{ m s}^{-1}$ ; full barb =  $5 \text{ m s}^{-1}$ ; flag =  $25 \text{ m s}^{-1}$ ). Surface-based CAPE and CIN (SBCAPE and SBCIN, respectively) and CAPE and CIN for a parcel having the mean potential temperature and water vapor mixing ratio of the lowest 1 km (MLCAPE and MLCIN, respectively) are indicated in the inset; the blue parcel process curve is for the surface-based parcel, though the mean-layer parcel's curve is nearly identical. The CAPE and CIN calculations include the effects of water vapor and assume pseudoadiabatic ascent. (b) Storm-relative hodograph derived from the 0131 UTC sounding [the observed mean storm motion of  $(12.6, 11.4) \text{ m s}^{-1}$  has been subtracted from the ground-relative wind profile]. The red (gray) hodograph is smoothed (unsmoothed). Numerals along the black hodograph trace indicate heights above ground level in kilometers. The 0–1-km SRH, 0–3-km SRH, and 0–6-km shear vector magnitude are indicated for the smoothed hodograph.

shown for the DOW7–NOXP radar pair owing to the fact that the cyclonic circulation center was only in the dual-Doppler lobe of that radar pair at a single analysis time (0148 UTC; not shown). Moreover, the large differences in the data horizons of the two radars, owing to the large differences in range from the circulation center ( $\sim 10 \text{ km}$  for NOXP vs  $\sim 35 \text{ km}$  for DOW7), are problematic for the three-dimensional wind synthesis.

The Doppler radar data were analyzed using the same methods as Markowski et al. (2012a,b), Marquis et al. (2012), and Kosiba et al. (2013). Edited radar data (ground clutter was removed and aliased velocities were dealiased during editing) were interpolated to a Cartesian grid moving with the mean velocity of the storm during the 0106–0140 UTC period [ $(12.6, 11.4) \text{ m s}^{-1}$ ]. The grid spans  $40 \text{ km} \times 40 \text{ km} \times 10 \text{ km}$  and has a 0.25-km grid spacing. The interpolation was performed using the two-pass Barnes's successive

corrections method (Barnes 1964; Koch et al. 1983; Majcen et al. 2008); the smoothing parameter  $\kappa$  was set to  $1.1 \text{ km}^2$  on the first pass and  $0.33 \text{ km}^2$  on the second pass.

The three-dimensional wind field was synthesized from the gridded radial velocity fields using an upward integration of the anelastic mass continuity equation, with the lower boundary condition being that the vertical velocity  $w$  vanishes there (i.e.,  $w = 0$  at  $z = 0$ ). Velocity data must be extrapolated downward in order to apply the lower boundary condition because  $z = 0$  is always below the radar data horizon ( $\sim 100$ – $600 \text{ m}$  below the radar horizon within the Clinton storm, depending on the time and exact location within the storm). The horizontal wind components at grid points below the data horizon were temporarily set equal to the wind components at the lowest overlying grid point where horizontal winds could be retrieved (the wind synthesis is performed iteratively).

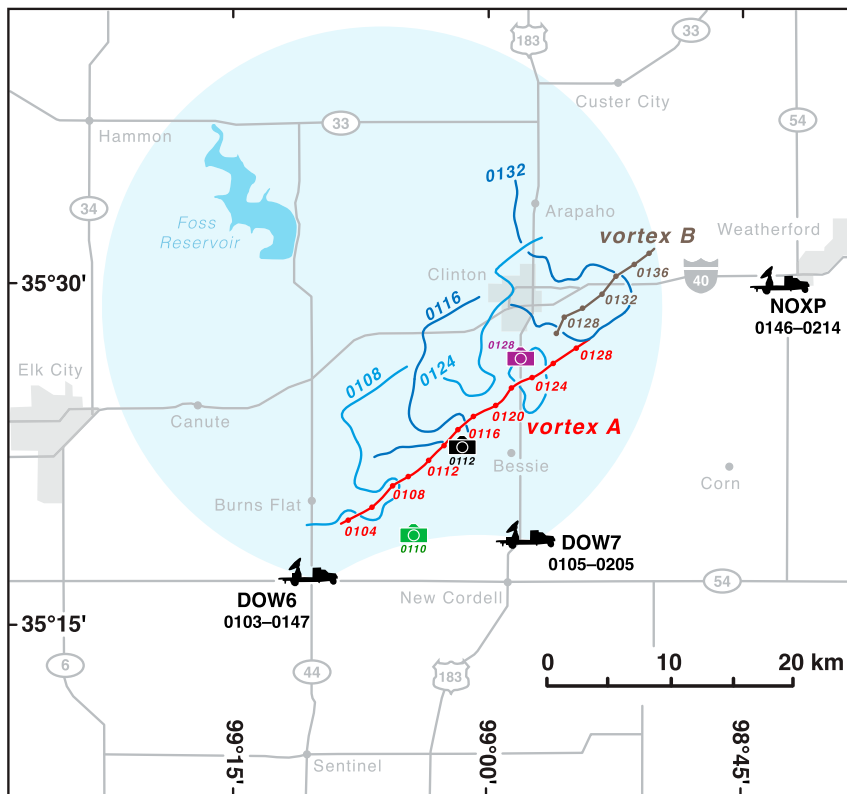


FIG. 4. The VORTEX2 deployment from 0103 to 0214 UTC 13 May 2010. Locations of the DOW6, DOW7, and NOXP radars, the dual-Doppler lobe used to retrieve the three-dimensional wind field from 0106 to 0138 UTC (light blue shading), and tracks of the near-surface circulation centers are indicated. The 20-dBZ reflectivity isopleth observed by DOW7 also is overlaid at 0108, 0116, 0124, and 0132 UTC (blue contours). The locations of the photographs that appear in Figs. 11a–c are indicated by the green, black, and purple camera icons, respectively (the photograph time are indicated beside the icons).

Downward extrapolation was forbidden during the gridding of radial velocity data using the aforementioned Barnes’s scheme. Once the three-dimensional wind synthesis was completed, all three velocity components at the grid points beneath the radar horizon were reset to “missing.” Three-dimensional wind velocities are available as low as the  $z = 0.25$ -km grid level at the beginning of the deployment (0106 UTC), but by the end of the deployment (0140 UTC), three-dimensional wind velocities are only available down to the  $z = 0.75$ -km grid level in the vicinity of the low-level mesocyclone owing to the increasing distance of the storm from the radar. Additional details pertaining to the analysis methodology can be found in Markowski et al. (2012a, their section 2a) and Marquis et al. (2012, their section 2b).

The analysis of the Clinton storm also includes retrievals of perturbation pressure at select times. The perturbation pressure fields on horizontal planes were

retrieved from the three-dimensional velocity fields following the techniques of Gal-Chen (1978) and Hane and Ray (1985), as in Markowski et al. (2012b). The retrieved pressure field at each altitude is only known to within an arbitrary horizontal constant, however. Without reliable, independent thermodynamic observations, this constant cannot be resolved and the vertical perturbation pressure gradient force (VPPGF) cannot be deduced. Unfortunately, as in several past dual-Doppler datasets of supercell storms (e.g., Beck et al. 2006; Wurman et al. 2007a,b, 2010; Marquis et al. 2008, 2012; Markowski et al. 2012a,b), buoyancy fields could not be reliably retrieved from the dual-Doppler wind syntheses owing to large errors. However, in controlled tests with synthetic radar data derived from a numerically simulated storm, Majcen et al. (2008) found that retrieved horizontal pressure fields were much more credible than retrieved horizontal buoyancy fields. Buoyancy retrievals are more error prone owing to their sensitivity to vertical gradients

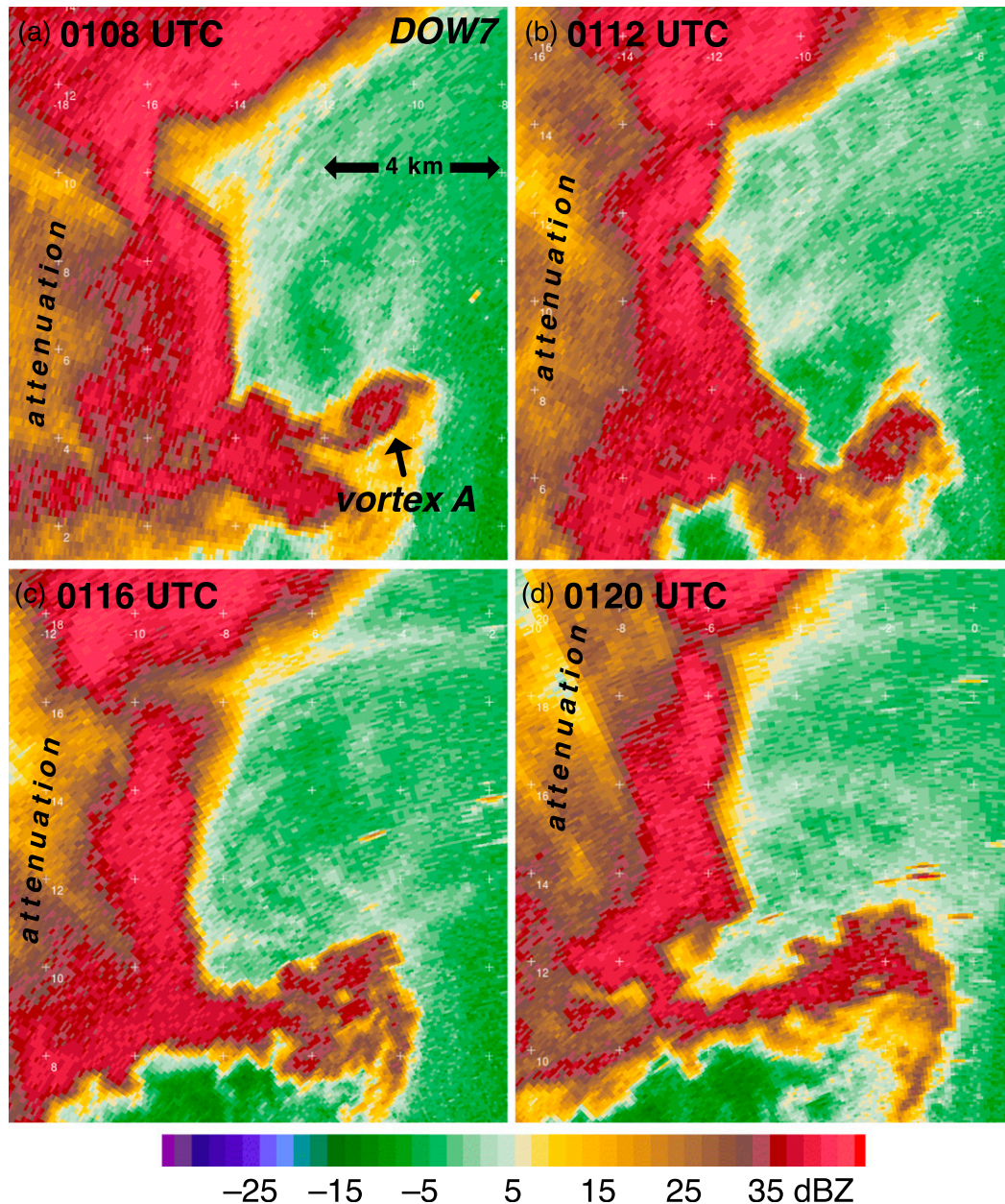


FIG. 5. Logarithmic reflectivity factor (dBZ) observed by DOW7 ( $0.4^{\circ}$ – $0.6^{\circ}$  elevation angles) at (a) 0108, (b) 0112, (c) 0116, (d) 0120, (e) 0124, (f) 0128, (g) 0132, and (h) 0136 UTC. The DOW7 reflectivity is uncalibrated. The purple camera icon in (f) indicates the location of the photograph in Fig. 11c.

of retrieved pressure (to within the aforementioned horizontal constant) and  $Dw/Dt$ .

#### b. Mobile mesonet data

Observations of temperature, relative humidity, pressure, and wind from six National Severe Storms Laboratory (NSSL) mobile mesonet probes (Straka et al. 1996; Vaughn and Fredrickson 2010), operating in collaboration with The Pennsylvania State University,

also were collected in limited areas within the storm until darkness ended operations at approximately 0130 UTC (the data were primarily obtained along the roads shown in Fig. 4). Mobile mesonet data were analyzed using the approach of Markowski et al. (2002), Shabbott and Markowski (2006), and Markowski et al. (2012a,b). High-frequency noise in the raw data was suppressed using two passes of a triangular filter having a 10-s radius, which significantly damps spatial

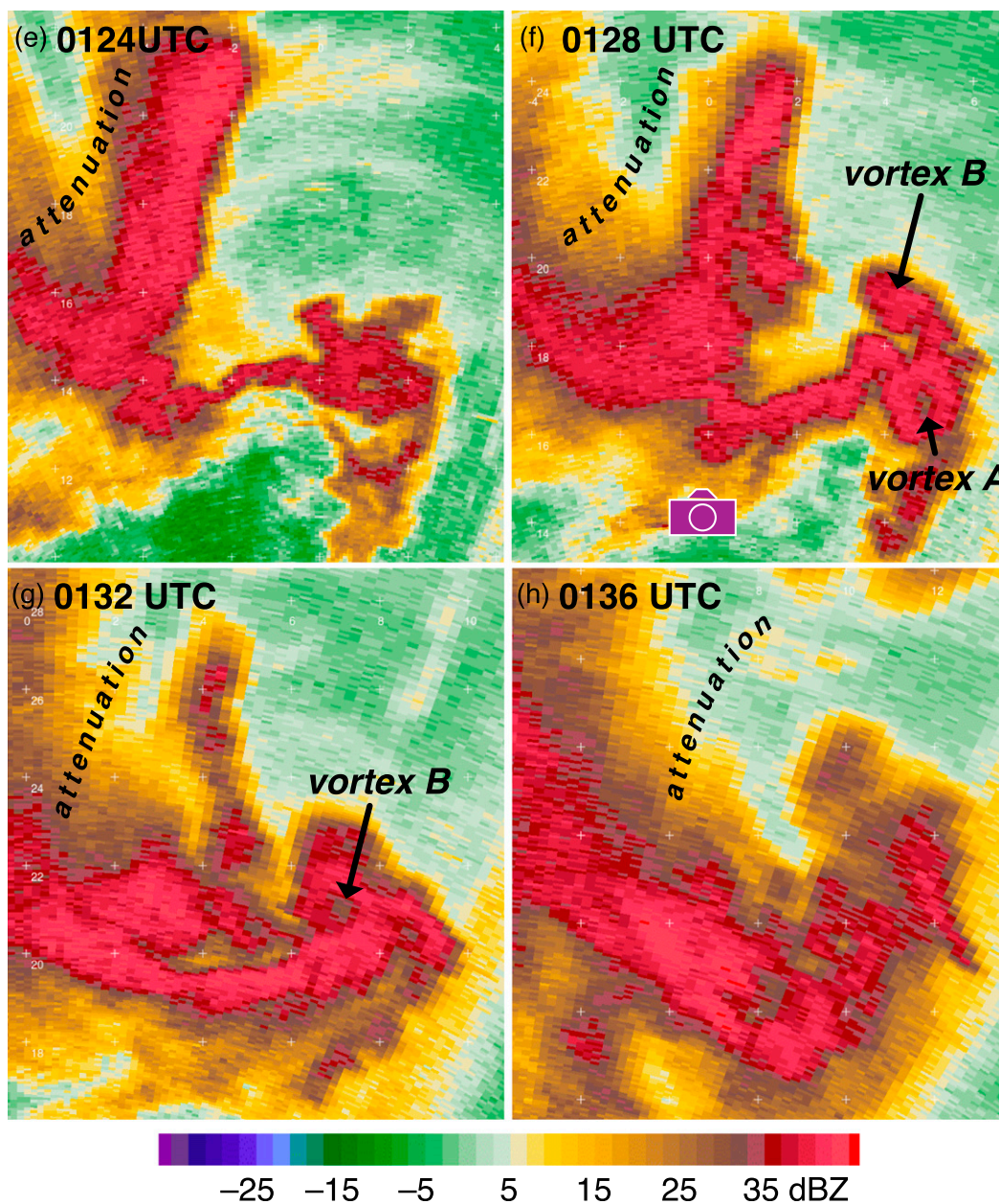


FIG. 5. (Continued)

scales less than  $\sim 0.3$  km (this assumes a vehicle speed of  $20\text{--}25\text{ m s}^{-1}$ ; the actual impact of the filtering on spatial scales depends on vehicle speed). Surface analyses were produced from time-space-converted smoothed observations spanning 10-min-wide windows centered on the analysis times. Observations closest to the reference time of each analysis were given the most weight in the drawing of the contours (over 80% of the observations appearing in the analyses were obtained within 2 min of the respective reference times). The raw observations are overlaid on each

analysis so that the reader may assess the credibility of the manually drawn contours.

### 3. The marginally tornadic period: 0106–0126 UTC

Throughout the first 20 min of dual-Doppler radar data collection, the Clinton storm exhibits a persistent “ball” of reflectivity at the tip of a hook echo (Figs. 5a–e and 6a–f). The ball of reflectivity is associated with rain curtains rotating about a marginally tornadic, generally broad cyclonic vortex, hereafter referred to as

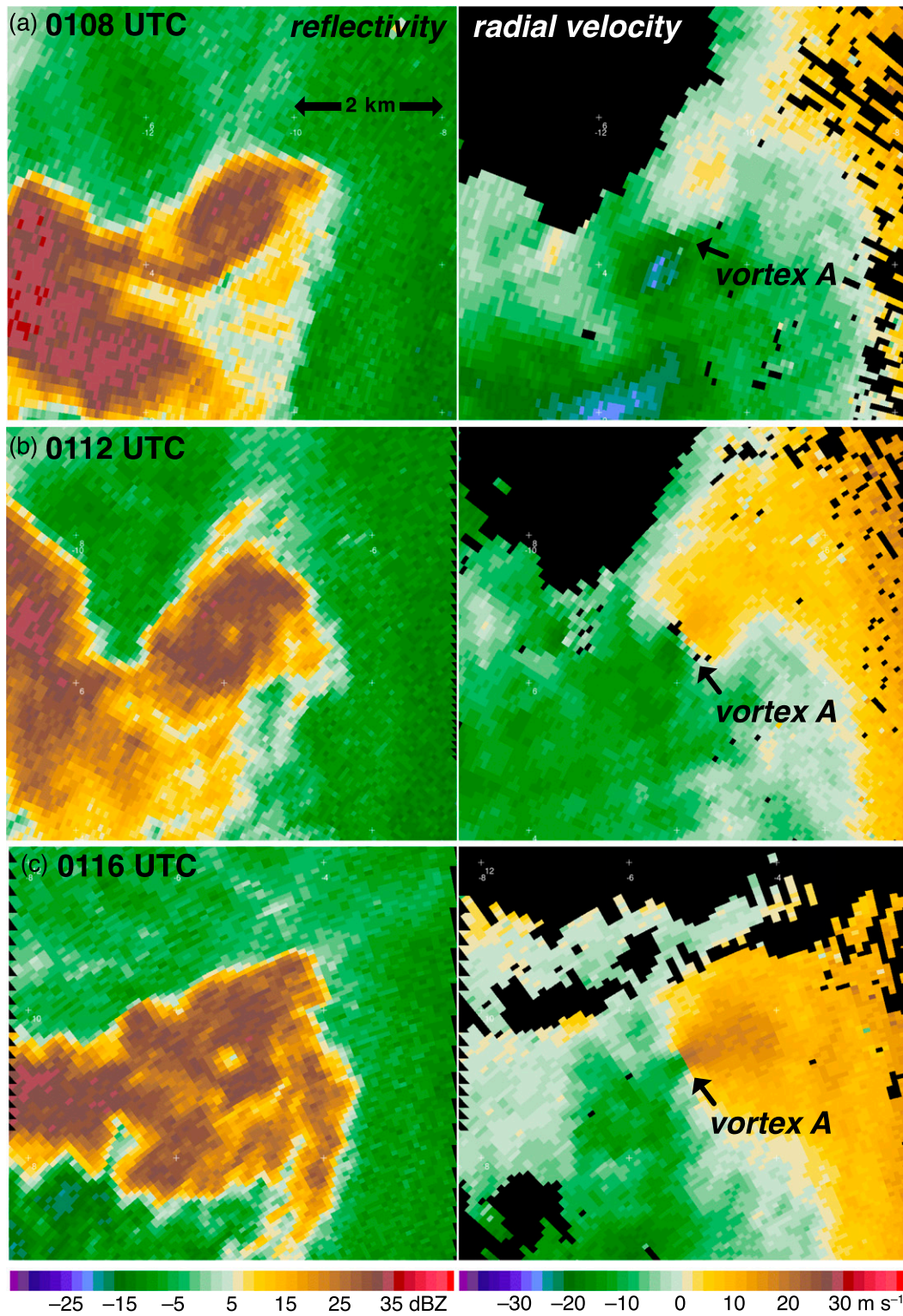


FIG. 6. Zoomed-in displays of logarithmic reflectivity factor (dBZ) and radial velocity ( $\text{m s}^{-1}$ ) observed by DOW7 ( $0.4^{\circ}$ – $0.6^{\circ}$  elevation angles) at (a) 0108, (b) 0112, (c) 0116, (d) 0120, (e) 0124, (f) 0126, (g) 0128, (h) 0130, (i) 0132, (j) 0134, (k) 0136, and (l) 0138 UTC. The DOW7 reflectivity is uncalibrated.

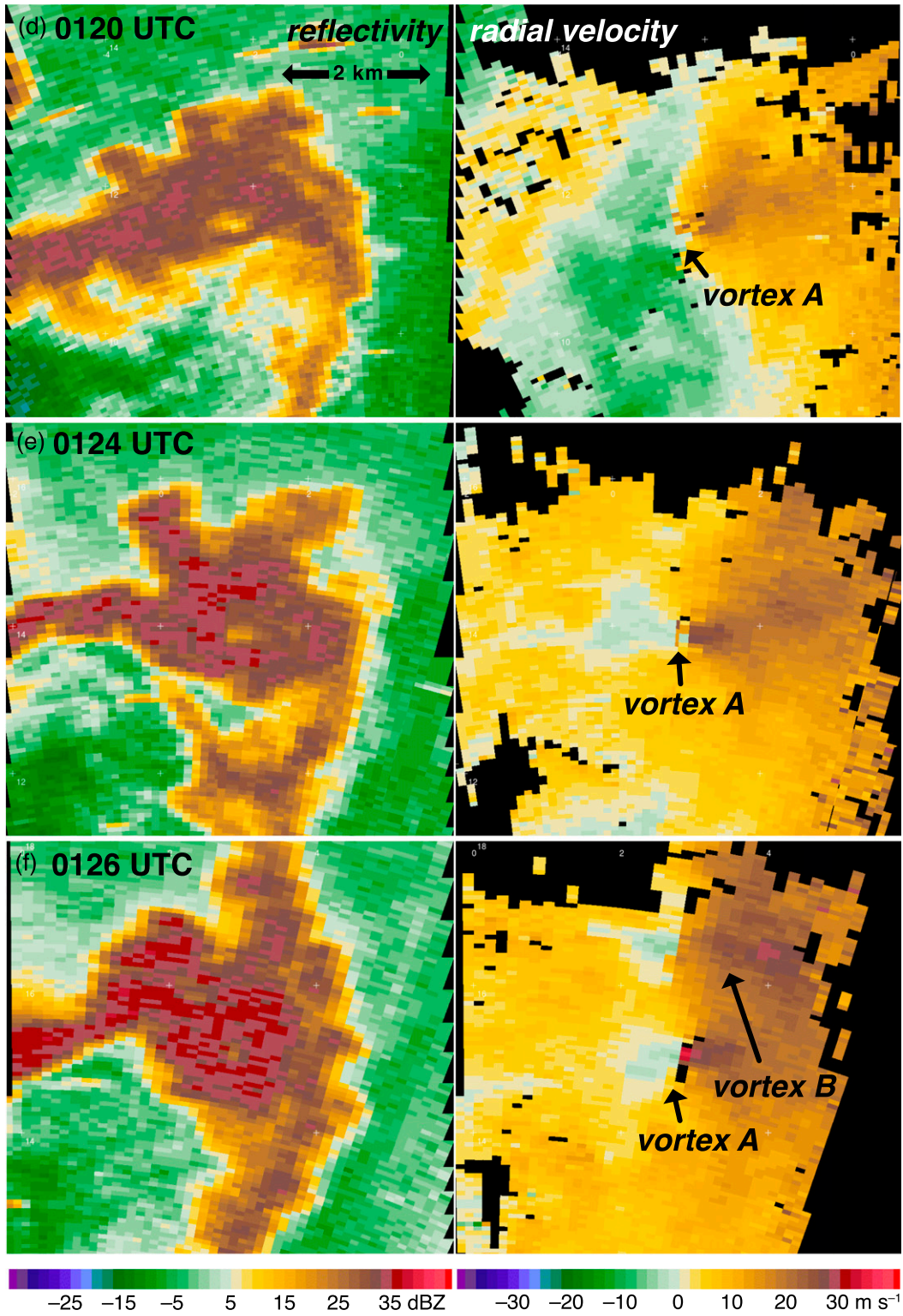


FIG. 6. (Continued)

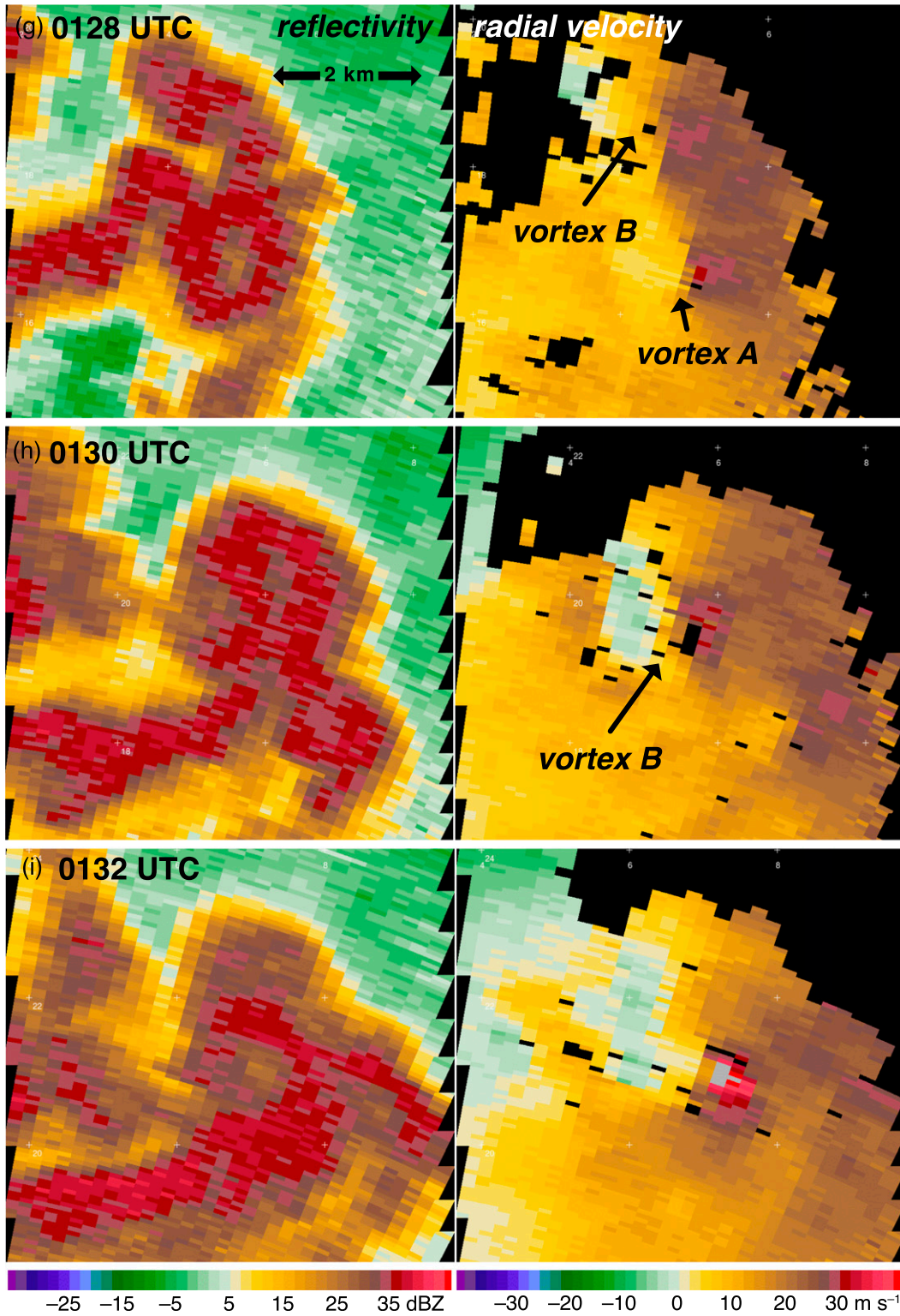


FIG. 6. (Continued)

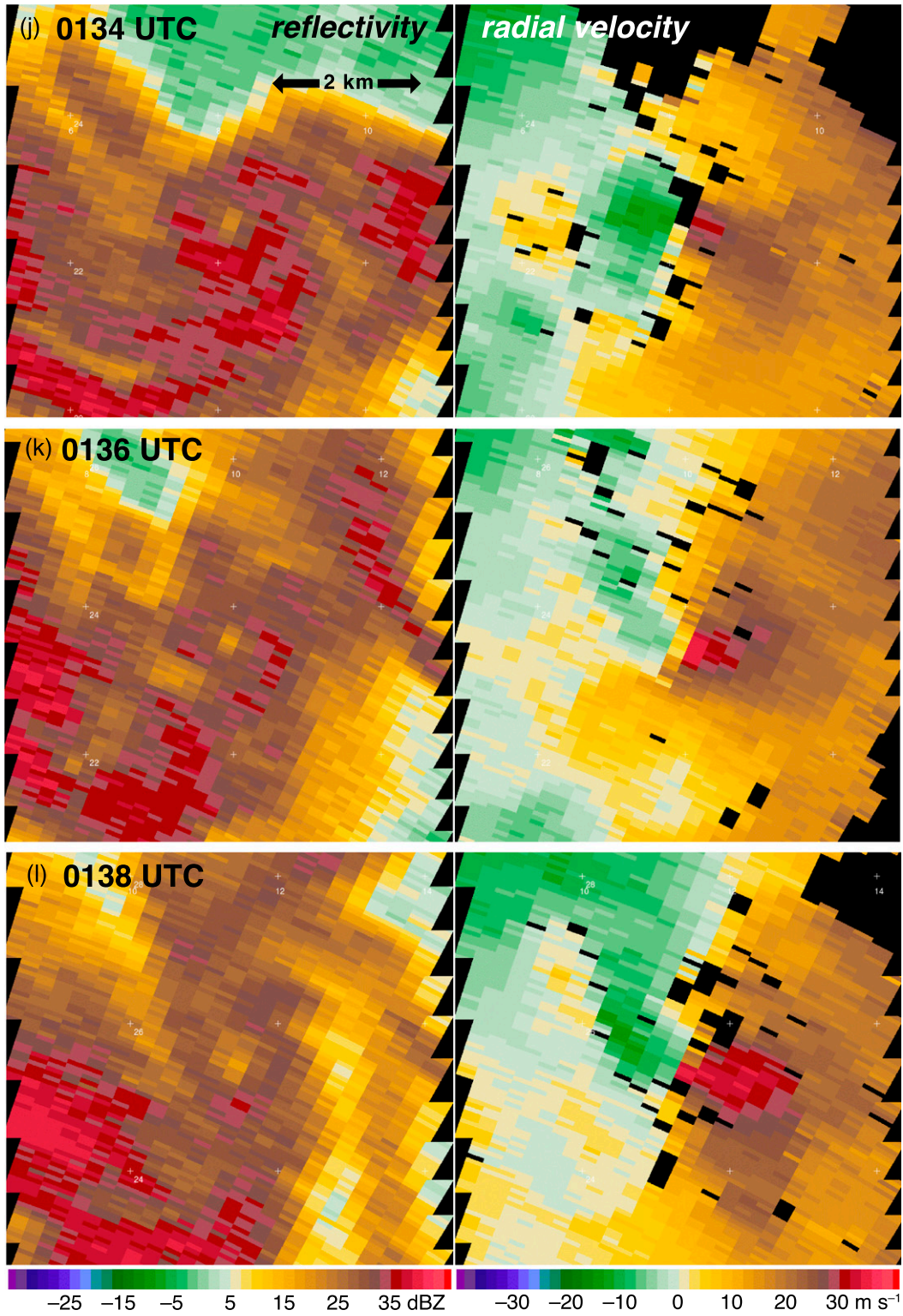


FIG. 6. (Continued)

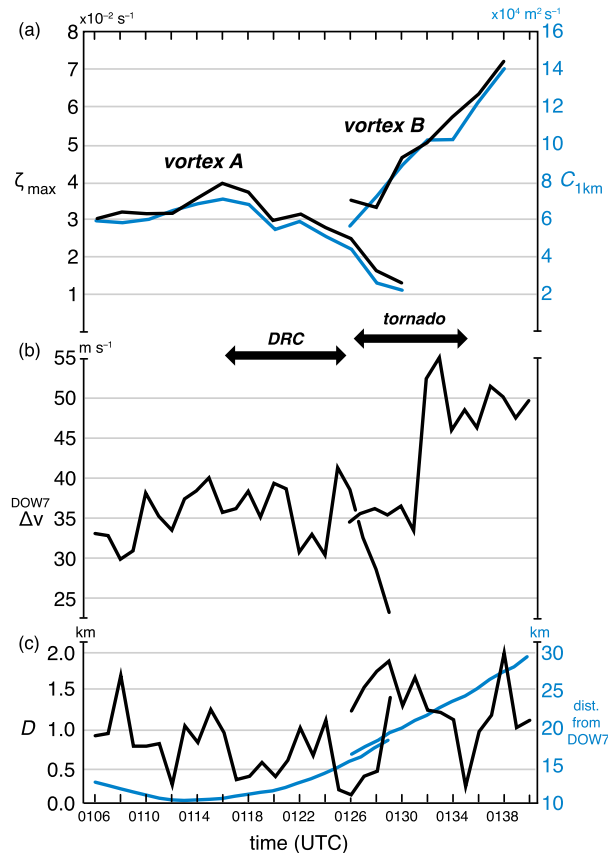


FIG. 7. (a) Time series of  $\zeta_{\max}$  (black) and circulation (blue) about a 1-km-radius ring centered on  $\zeta_{\max}$  at  $z = 0.75$  km, derived from the dual-Doppler wind syntheses, for vortex A and vortex B. (b) Time series of the maximum radial velocity differential  $\Delta v$  observed on the lowest scan by DOW7 for vortex A and vortex B. (c) Time series of the distance  $D$  between the maximum inbound and maximum outbound radial velocities (black) and distance from the radar (blue). The time period of the tornado is based on the official record in *Storm Data*.

vortex A.<sup>3</sup> During most of this period, a small weak-echo eye is also visible within the reflectivity ball, similar to those that have been associated with tornadoes previously observed in mobile radar data (e.g., Wurman et al. 1996; Bluestein and Pazmany 2000). The maximum inbound–outbound radial velocity differential ( $\Delta v$ ) of vortex A varies from 30 to 42 m s<sup>−1</sup> during this time period (Fig. 7b), as observed by DOW7 (DOW6 is generally farther from the vortex and detects a weaker  $\Delta v$ , though the trends of the DOW6  $\Delta v$  observations are qualitatively similar). The distance

<sup>3</sup> Although reflectivity balls are often attributed to debris (so-called debris balls), reflectivity balls are commonly observed in mobile radar data, even in nontornadic circulations, owing to rotating rain curtains.

between the maximum inbound and outbound radial velocities is approximately 0.6 km on average, though it varies from as little as 0.2 km to as much as 1.7 km from 0106 to 0126 UTC (Fig. 7c). The relative noisiness in both  $\Delta v$  and the diameter of the inbound–outbound velocity couplet is probably more due to sampling vagaries rather than true changes in intensity or structure.

The trend in the maximum vertical vorticity ( $\zeta_{\max}$ ) derived from the dual-Doppler wind fields (which are, of course, smoother than the raw radial velocity observations used to compute  $\Delta v$ ), features a gradual increase in  $\zeta_{\max}$  from 0106 to 0116 UTC, during which time  $\zeta_{\max}$  at  $z = 0.75$  km increases from 0.030 to 0.040 s<sup>−1</sup>, followed by a weakening trend through the remainder of the marginally tornadic period (Figs. 7a and 8a–f). By 0126 UTC,  $\zeta_{\max}$  at  $z = 0.75$  km decreases to 0.025 s<sup>−1</sup>, with further weakening of vortex A occurring beyond that time (section 4). The location of  $\zeta_{\max}$  is generally 1–3 km southeast of a relative maximum in  $w$  that is detached from the main updraft region. This is evident in both the horizontal cross sections of  $\zeta$  and  $w$  at  $z = 0.75$  km (Figs. 8a–f), as well as in three-dimensional perspectives of  $\zeta$  and  $w$  isosurfaces (Figs. 9a–c).

Mobile mesonet observations prior to 0120 UTC are mostly confined to the rear-flank outflow and inflow regions (Fig. 10a), but in the 0120–0126 UTC period, observations also are available within 2 km of the location of  $\zeta_{\max}$  (Figs. 10b,c). Potential temperature perturbations  $\theta'$  of  $-2$  to  $-3$  K were sampled in the outflow that trails the hook echo at 0112 UTC (Fig. 10a), with colder air ( $\theta'$  as low as  $-4$  K) detected at 0126 UTC (Fig. 10c), albeit somewhat far to the west of the circulation center.<sup>4</sup> Warmer air was sampled nearer to the circulation center, where  $\theta'$  is  $\geq -1.5$  K in the 0120–0126 UTC period (Fig. 10b). The wet-bulb potential temperature  $\theta_w$  of this air ( $\sim 21.7^\circ\text{C}$ ) is very nearly identical to that of the inflow immediately east of the gust front, implying that these air parcels have significant CAPE despite being on the cool side of the gust front and within the rotating rain curtains of the

<sup>4</sup> Density potential temperature perturbations ( $\theta'_\rho$ ; Emanuel 1994, p. 161) are a better measure of the buoyancy of the air, but there is too much uncertainty in the condensate mass to compute this accurately, especially given the uncalibrated radar reflectivity. Moreover, relative humidity observations are unavailable from one of the mobile mesonet vehicles (Probe 2); thus, virtual potential temperature perturbations ( $\theta'_v$ ) also cannot be analyzed. For this reason,  $\theta'$  is analyzed in Fig. 10. Though the differences between  $\theta'_\rho$  and  $\theta'$  could exceed 1 K in moderate precipitation, the differences between  $\theta'_v$  and  $\theta'$  are only  $\sim 0.1$  K for the observations for which relative humidity is available.

vortex (Fig. 3). Photographs of the Clinton storm taken from two of the mobile mesonet vehicles at 0110:20 and 0112:00 UTC reveal, respectively, the updraft of the Clinton storm viewed from the south-southeast and a wall cloud associated with the marginally tornadic circulation viewed from the east-northeast (Figs. 11a,b).

The key development that seems linked to the weakening trend in  $\zeta$  beginning at 0116 UTC is the development of a DRC, similar to the ones documented by Rasmussen et al. (2006), Kennedy et al. (2007a,b), Byko et al. (2009), and Markowski et al. (2012a). The DRC is first detected at 0116 UTC, at an altitude of approximately 3 km, as a downward protrusion of the 35-dBZ reflectivity isosurface observed by DOW7 (Fig. 9b). The DRC subsequently descends to the surface along the northern flank of the cyclonic vorticity column (Figs. 9b–d), and reaches the elevation of the lowest radar scans at 0120 UTC. Although unmistakable in reflectivity isosurfaces, the enhancement of reflectivity in the hook echo associated with the DRC is subtle in horizontal cross sections (Figs. 6d–f and 8d–f). Reflectivity in the DRC continues to increase from 0120 to 0124 UTC, eventually exceeding 40 dBZ (Figs. 9d–f). The descent of the DRC is accompanied by an abrupt weakening of vortex A from the bottom-up from 0116 to 0126 UTC (Figs. 8c–f and 9b–g), marking the end of the marginally tornadic period.

Given that the appearance of the DRC follows an amplification, albeit gradual, of low-level  $\zeta$  between 0106 and 0116 UTC, and descends in such close proximity to the axis of rotation, the DRC appears to be of the type-III variety as classified by Byko et al. (2009)—that is, the variety that results from the amplification of near-surface  $\zeta$  and an attendant downward-directed dynamic VPPGF. Although we could not retrieve the dynamic VPPGF field and establish that it indeed points downward prior to the development of the DRC, a pressure minimum was retrieved at  $z = 0.75$  km less than a kilometer south of the DRC (Fig. 12a), and the  $\zeta$  isosurfaces in the 0114–0118 UTC period reveal that  $\zeta$  decreases with height in the vicinity of DRC development (Figs. 9a–c).

To assess the forcings responsible for the changes in the intensity of vortex A, we resort to an Eulerian analysis of circulation in a horizontal plane,  $C = \oint \mathbf{v}_h \cdot d\mathbf{l}$ , where  $\mathbf{v}_h$  is the horizontal velocity vector and  $d\mathbf{l}$  is a vector line element of the circuit about which  $C$  is computed.<sup>5</sup>

<sup>5</sup> We do not distinguish between relative and absolute circulation because they are very nearly the same. The contribution to the absolute circulation from planetary vorticity (equal to  $\pi r^2 f$ , where  $r$  is the radius of the ring and  $f$  is the Coriolis parameter) is two orders of magnitude smaller than the relative circulation for the 1-km-radius rings.

Circulation  $C$  is evaluated about 1-km-radius rings centered on  $\zeta_{\max}$  at  $z = 0.75$  km, which is the lowest altitude at which three-dimensional winds are available throughout the entire dual-Doppler deployment (i.e., from 0106 to 0140 UTC). The  $C$  about a ring in the horizontal plane is proportional to the area-averaged  $\zeta$  within the ring. For the relatively small rings used, the time series of  $C$  closely follows the time series of  $\zeta_{\max}$  (Fig. 7a), though calculations of forcings for  $C$  are less volatile than calculations of forcings for  $\zeta_{\max}$ , owing to the averaging involved in the former. A Lagrangian analysis of  $C$  about material circuits, like that performed by Markowski et al. (2012b), also would have been desirable. It would have allowed for the evaluation of the relative contributions of barotropic versus non-barotropic (i.e., baroclinic and/or frictionally generated vorticity) sources of vorticity/circulation to the low-level mesocyclone. Unfortunately, such an analysis could not be performed owing to a wide swath of missing velocity data northeast of the hook echo and low-level mesocyclone of the Clinton storm, within the outflow but east and south of the precipitation, where reflectivity was weak (e.g., Figs. 6 and 8). (Backward trajectories originating near the low-level mesocyclone quickly enter the region of missing velocity data.)

Neglecting viscosity, the convergence of planetary vorticity, and solenoidal generation (the latter vanishes in the anelastic limit), local changes in circulation are governed by

$$\frac{\partial C}{\partial t} = - \oint \zeta \mathbf{v}_h \cdot \mathbf{n} dl + \oint \boldsymbol{\omega}_h \cdot \mathbf{n} dl, \quad (1)$$

where  $\boldsymbol{\omega}_h$  is the horizontal vorticity vector and  $\mathbf{n}$  is the unit vector normal to the ring, directed outward. Given that the analysis grid moves with the storm and its mesocyclone,  $\partial C/\partial t$  and  $\mathbf{v}_h$  are in a storm-relative reference frame. Trapp and Weisman (2003) refer to the two terms on the rhs of (1) as the  $\zeta$  flux and  $\boldsymbol{\omega}$  flux. The  $\zeta$  flux is equal to the sum of vertical vorticity stretching ( $\zeta \partial w/\partial z$ ) and horizontal advection ( $-\mathbf{v}_h \cdot \nabla_h \zeta$ ), averaged within the control area. The  $\boldsymbol{\omega}$  flux is equal to area-averaged tilting of  $\boldsymbol{\omega}_h$  into the vertical ( $\boldsymbol{\omega}_h \cdot \nabla_h w$ ) plus area-averaged vertical advection of  $\zeta$  ( $-w \partial \zeta/\partial z$ ). Vertical stretching of  $\zeta$  and horizontal (inward, radial) advection of  $\zeta$  by  $\mathbf{v}_h$  tend to be anticorrelated at low altitudes, as do the tilting of  $\boldsymbol{\omega}_h$  into the vertical and vertical advection of  $\zeta$ . A positive  $\zeta$ -flux forcing usually implies positive vertical stretching of  $\zeta$  that exceeds a negative horizontal advection of  $\zeta$ . Likewise, a positive  $\boldsymbol{\omega}$ -flux forcing usually implies a conversion of horizontal vorticity into cyclonic vorticity via tilting that exceeds

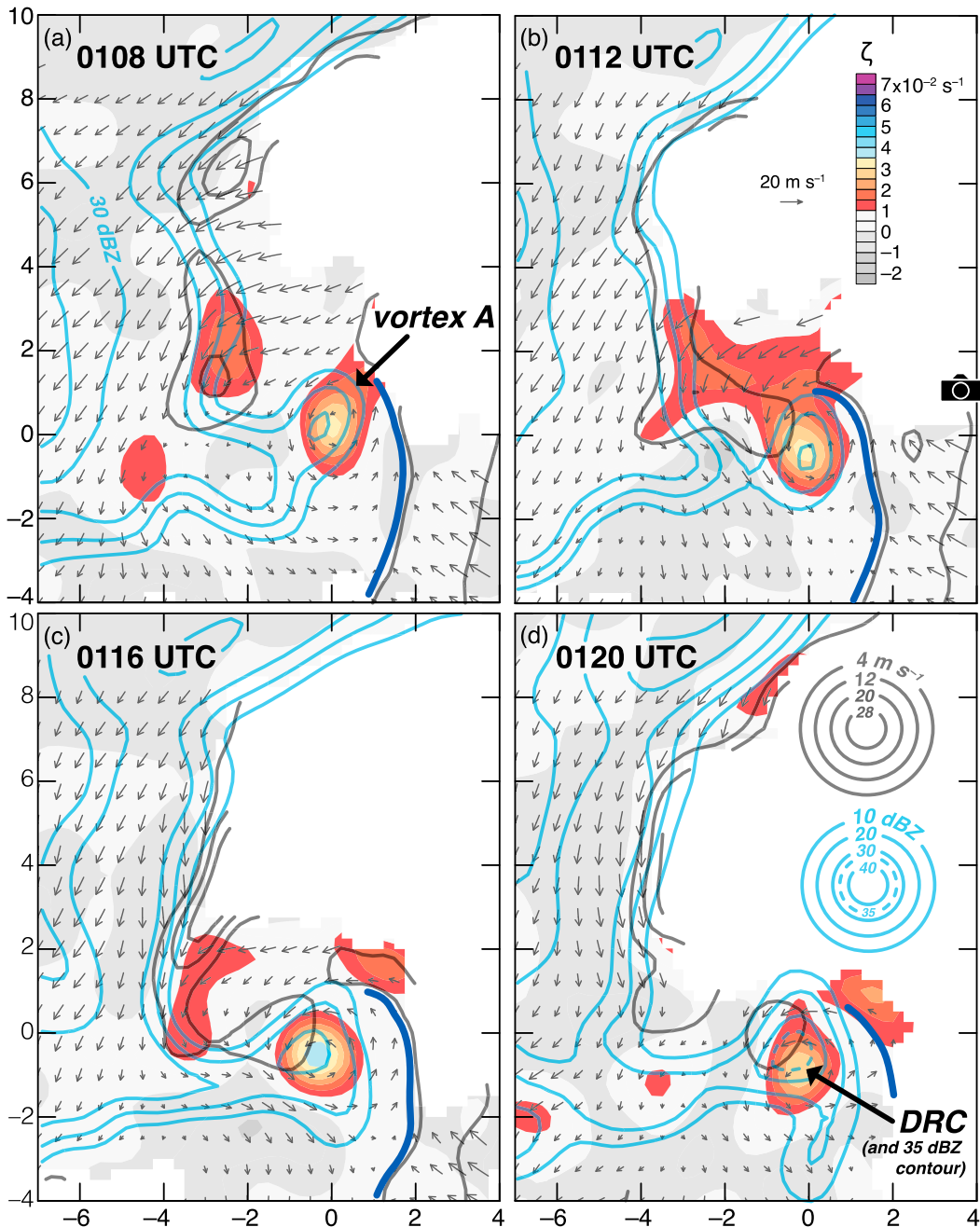


FIG. 8. Horizontal cross sections of vertical vorticity (color shading), vertical velocity (dark gray contours every  $8 \text{ m s}^{-1}$  starting at  $4 \text{ m s}^{-1}$ ), and storm-relative horizontal wind vectors (every third grid point) at  $z = 0.75 \text{ km}$  obtained from the dual-Doppler wind syntheses at (a) 0108, (b) 0112, (c) 0116, (d) 0120, (e) 0124, (f) 0126, (g) 0128, (h) 0130, (i) 0132, (j) 0134, (k) 0136, and (l) 0138 UTC. The objectively analyzed (uncalibrated) logarithmic reflectivity factor from DOW7 also is overlaid in each panel (light blue contours of 10, 20, 30, 35, and 40 dBZ; the intermediate 35-dBZ contour is dashed). Gust front locations are indicated with the heavy blue line in (a)–(d). The black camera icon in (b) indicates the location of the photograph in Fig. 11b. The purple camera icon in (g) indicates the location of the photograph in Fig. 11c.

the negative vertical advection of  $\zeta$ . Budgets of  $\partial C/\partial t$  were found to be better reconciled when the forcings on the rhs of (1) were computed as line integrals as opposed to area-averaging fields of vorticity stretching,

tilting, and advection, which contain more derivatives than the  $\zeta$ - and  $\omega$ -flux terms in (1).

The integrated  $\omega$  flux is positive and nearly constant throughout the intensification of vortex A from 0106

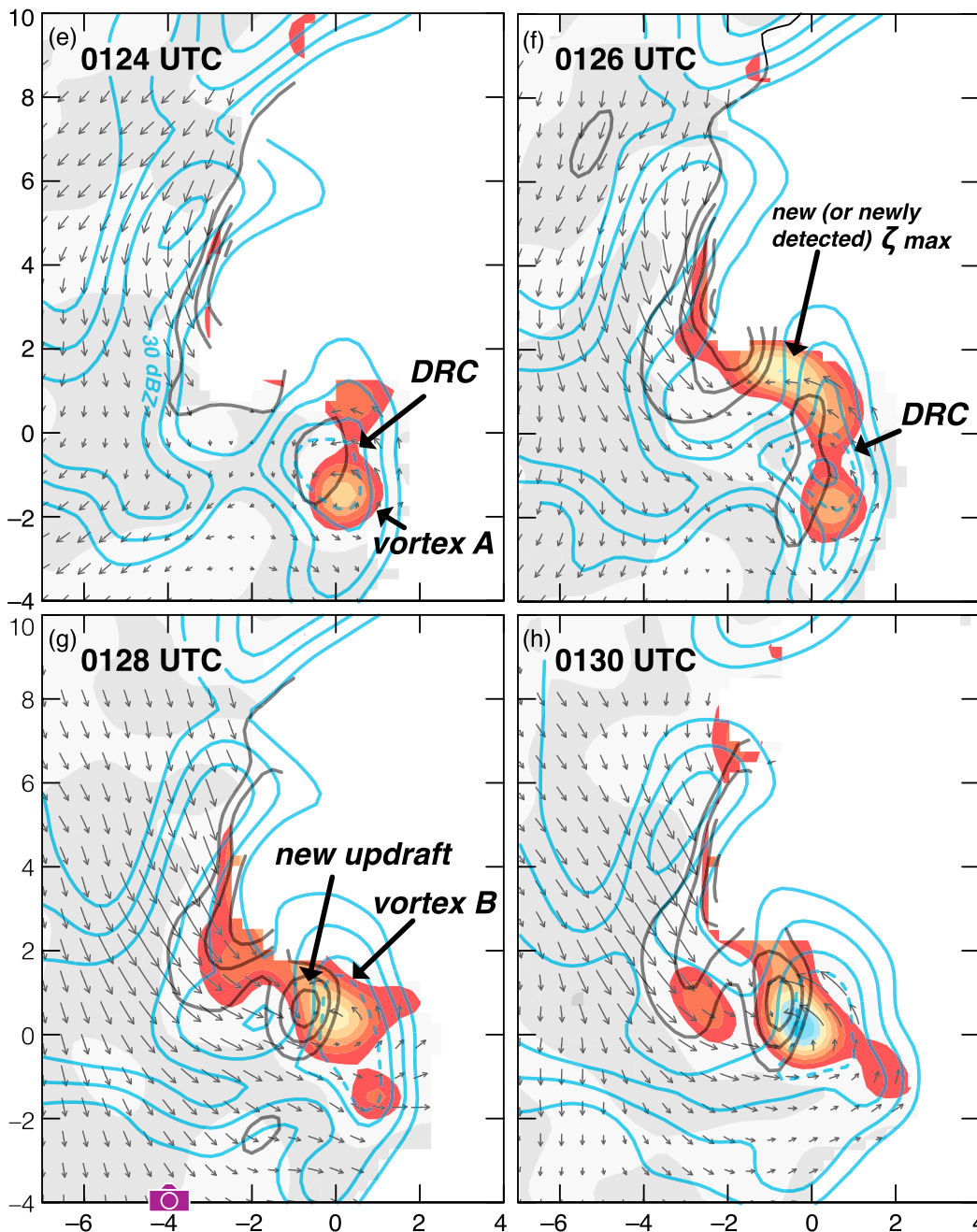


FIG. 8. (Continued)

to 0116 UTC (i.e., when  $\partial C/\partial t > 0$ ), as well as through at least the early part of its demise (the  $\omega$  flux remains positive until 0124 UTC) (Fig. 13). The forcing for  $C$  from the  $\zeta$  flux, however, is negligible from 0106 to 0108 UTC, positive during the period of most rapid intensification of  $C$  (and  $\zeta_{\max}$ ) from 0110 to 0114 UTC, becomes small once again at 0116 UTC, and then becomes strongly negative thereafter, as the DRC arrives at low levels. Vortex A subsequently weakens.

In other words, the DRC's appearance at 0116 UTC is accompanied by an immediate reversal in the sign of the  $\zeta$ -flux forcing for  $C$  and trend in  $C$ —the fate of vortex A is strongly linked to the evolution of stretching. (Later, after 0122 UTC, the  $\omega$ -flux forcing eventually goes negative as well.) The budget calculations appear to be reliable. The trends of the sum of the  $\zeta$ -flux and  $\omega$ -flux forcings closely follow the trends in the observed  $\partial C/\partial t$ , though the sum of the forcings

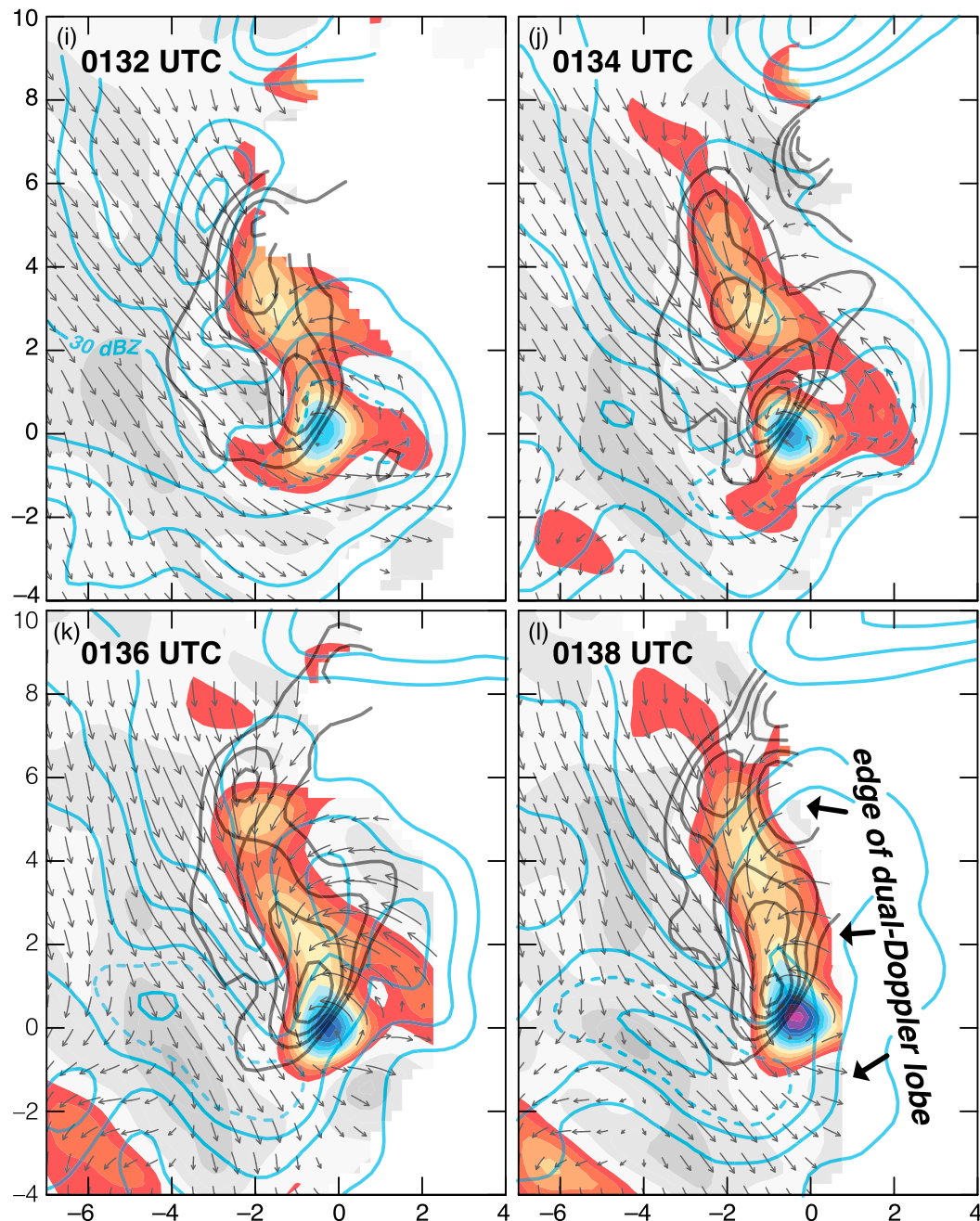


FIG. 8. (Continued)

is consistently  $20\text{--}30\text{ m}^2\text{ s}^{-2}$  more positive than the observed  $\partial C/\partial t$ . This bias is unsurprising given the omission of viscous effects from the calculation of the forcings for  $\partial C/\partial t$ .

#### 4. The tornadic period: 0126–0140 UTC

Although the development of the DRC midway through the marginally tornadic period appears to have

fostered the demise of vortex A, a new vortex, hereafter vortex B, rapidly developed immediately north of the DRC in the minutes that followed (Figs. 6f–l and 8f–l). The first clear indication of a new  $\zeta$  maximum in the DOW7 radial velocity field and dual-Doppler-derived wind fields is at 0126 UTC (Figs. 6f and 8f), though we cannot discount the possibility of its presence at least a little earlier, given the proximity of the new  $\zeta$  maximum to the edge of the data boundary

(recall that usable wind data did not extend far beyond the regions of high reflectivity and precipitation). [There is a suggestion of enhanced  $\zeta$  along the data boundary in Fig. 8e near (0.5, 0.5).]

The vortex rapidly intensifies, and by 0130 UTC, a new ball of high reflectivity, with a weak-echo eye, develops at the tip of the hook echo (Fig. 6h). DOW7 maximum  $\Delta v$  values jump from 33 to 52  $\text{m s}^{-1}$  from 0131 to 0132 UTC (Fig. 7b). The older reflectivity ball and eye that had been associated with vortex A quickly dissipate between 0128 and 0132 UTC (Figs. 6g–i and 7a,b), though a brief funnel cloud was photographed at 0128:40 UTC in association with the weakening vortex A (Fig. 11c). No debris was observed beneath the funnel cloud, and it was too far from the nearest radar (DOW7) to be resolved (the DOW7  $\Delta v$  was 28  $\text{m s}^{-1}$  at this time at the location of vortex A; Fig. 7b). The funnel cloud was south of an opaque rain shaft associated with the hook echo, within which reflectivity is increasing at this time, preventing a view of vortex B from the location of the photograph in Fig. 11c (also refer to Figs. 4 and 5f). A well-defined “clear slot” in the cloud base (an indication of a strengthening rear-flank downdraft), on the southern fringe of the hook echo, also is evident from the location of the photograph.

The tornado lifetime is listed as 0126–0135 UTC in *Storm Data*. Given the lack of visibility in the vicinity of vortex B [the Probe 2 mobile mesonet crew was best positioned, but their view was blocked by intervening precipitation (Fig. 11c)] and distance from the nearest radar (the DOW7  $\Delta v$  at 0126 UTC was 35  $\text{m s}^{-1}$ , but the radar was 17.5 km from the vortex; Figs. 7b,c), we cannot refute the officially reported start time. As for the ending time, 0135 UTC also is plausible even though we cannot specify the exact ending time of the tornado. No visual observations of the tornado were made owing to darkness and the extensive precipitation that surrounded the vortex, unfortunately. Although the maximum  $\Delta v$  observed by DOW7 remains above 45  $\text{m s}^{-1}$  until the cessation of DOW7 operations at 0140 UTC (Figs. 6k,l and 7b), it is unlikely that DOW7 is resolving the tornado given its range of 20–30 km during this window (Fig. 7c). In the coarser three-dimensional wind fields retrieved from the dual-Doppler observations,  $\zeta$  increases steadily from 0126 to 0138 UTC (0138 UTC marks the end of dual-Doppler data collection), but of course, the tornado is not resolved on the wind synthesis grids either. The NOXP radar began scanning the storm at 0146 UTC from a position 10 km to the southeast (Fig. 4). On the initial base scan (1° elevation angle, which was  $\sim 0.15$  km AGL), the radar detected a strong but broad cyclonic

circulation having a  $\Delta v$  of 46  $\text{m s}^{-1}$  over a horizontal distance of 1.2 km (Fig. 14). No strong “gate-to-gate” shear was detected during its scanning from 0146 to 0214 UTC that would have strongly suggested the presence of a tornado.

The DRC that is observed from 0116 to 0126 UTC, which coincides with the rapid weakening of vortex A, may have helped trigger the rapid intensification of vortex B and tornadogenesis. Although the midlevel mesocyclone in the main updraft of the Clinton storm intensifies between 0122 and 0124 UTC (Figs. 9e,f) for reasons we cannot ascertain and that have no obvious connection to the DRC, the DRC appears to have been a factor in the initiation of a new updraft “pulse.” The new updraft pulse is first visible at 0126 UTC in the depiction of the  $w$  isosurfaces (Fig. 9g), and is evident in the horizontal cross sections of  $w$  by 0128 UTC (Fig. 8g). The  $\zeta = 0.035\text{-s}^{-1}$  isosurface also extends downward toward the lowest kilometer within the updraft pulse by 0128 UTC (Fig. 9h). A strong upward-directed dynamic VPPGF likely is present in the lowest kilometer beneath the downward-protruding, high- $\zeta$  isosurface, owing to the large  $\partial\zeta^2/\partial z$  implied here (Markowski and Richardson 2014; Coffey and Parker 2017). The updraft pulse rapidly intensifies, with  $w > 20 \text{ m s}^{-1}$  extending below  $z = 0.75$  km in the dual-Doppler-retrieved  $w$  field (Figs. 8g–i and 9h,i). The updraft pulse eventually “merges” with the main updraft (Figs. 9j–l). The low-level updraft is 3–4 times stronger in the vicinity of  $\zeta_{\text{max}}$  than it had been during the marginally tornadic phase summarized in section 3, during which time  $w$  at  $z = 0.75$  km rarely exceeded 6  $\text{m s}^{-1}$  in the vicinity of  $\zeta_{\text{max}}$  (Figs. 8a–f).

The collocation of an intense low-level updraft and antecedent circulation leads to an explosion of grid-resolved  $\zeta$  from 0126 to 0140 UTC. In terms of the forcings for area-averaged  $\zeta$  within a 1-km-radius ring centered on  $\zeta_{\text{max}}$  given by (1), both the  $\zeta$ -flux and  $\omega$ -flux forcings are very large, much larger than at any point in the lifetime of vortex A (Fig. 13). This is all that can be concluded about the budget, given that the  $C$  budget reconciliation is poor. The poor reconciliation could be the result of a large viscous contribution or large errors in the retrieved three-dimensional wind fields given the long range from the radars (longer than for vortex A). As the data horizon rises owing to increasing range, a greater degree of downward extrapolation of horizontal convergence below the radar horizon is required in order to perform the wind synthesis.

The possible influence of the DRC in promoting the new updraft pulse and subsequent intensification of rotation is perhaps best seen in the retrieved pressure

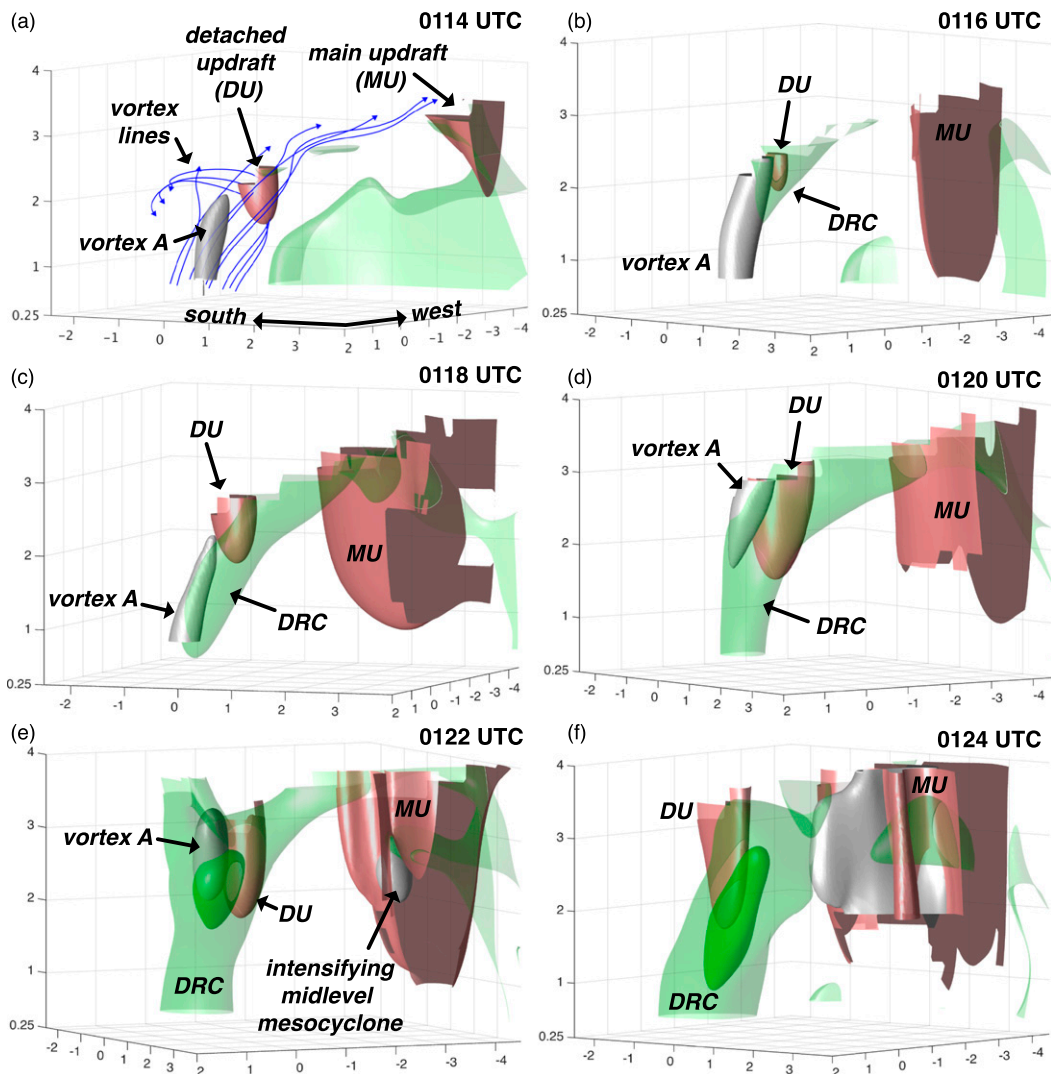


FIG. 9. Three-dimensional view, from the northeast, of the 35- and 40-dBZ DOW7 reflectivity isosurfaces (light green and dark green),  $20 \text{ m s}^{-1}$  vertical velocity isosurfaces (light red), and  $0.035 \text{ s}^{-1}$  vertical vorticity isosurfaces (gray) at (a) 0114, (b) 0116, (c) 0118, (d) 0120, (e) 0122, (f) 0124, (g) 0126, (h) 0128, (i) 0130, (j) 0132, (k) 0134, and (l) 0136 UTC. In (a), at 0114 UTC, some vortex lines (blue) also are plotted (these are discussed in section 5). In (g), at 0126 UTC, the  $10 \text{ m s}^{-1}$  vertical velocity isosurface also is shown (very pale red) in order to better reveal the initiation of the new updraft referred to in the text. In (i)–(l), during the 0130–0136 UTC period, reflectivity isosurfaces are omitted in order to improve figure clarity.

field in the vicinity of the DRC. At 0126 UTC, the DRC is associated with a relative maximum in pressure, with horizontal pressure gradient force (HPGF) field lines pointing northward on the northern flank of the DRC and southward on the southern flank of the DRC (Fig. 12b). Although we could not reliably retrieve the buoyancy field or VPPGF field (the latter would allow three-dimensional perturbation pressure gradient force field lines), the HPGF field lines are consistent with field lines we might expect surrounding a column of negative buoyancy, at least if the buoyancy

perturbation pressure is not dwarfed by the dynamic perturbation pressure (Houze 1993, p. 225). The HPGF field lines would imply forcing for low-level updraft in the regions north and south of the DRC. Indeed, the DRC is collocated with negative  $\partial w/\partial t$ , and is flanked (north and south) by positive  $\partial w/\partial t$  centers ( $\partial w/\partial t$  is computed via centered-in-time finite-differencing of the vertical velocity fields). (Figure 12 displays  $\partial w/\partial t$  as a measure of updraft forcing, rather than  $Dw/Dt$ , owing to the fact that the latter is much more error prone, particularly the calculation of nonlinear vertical

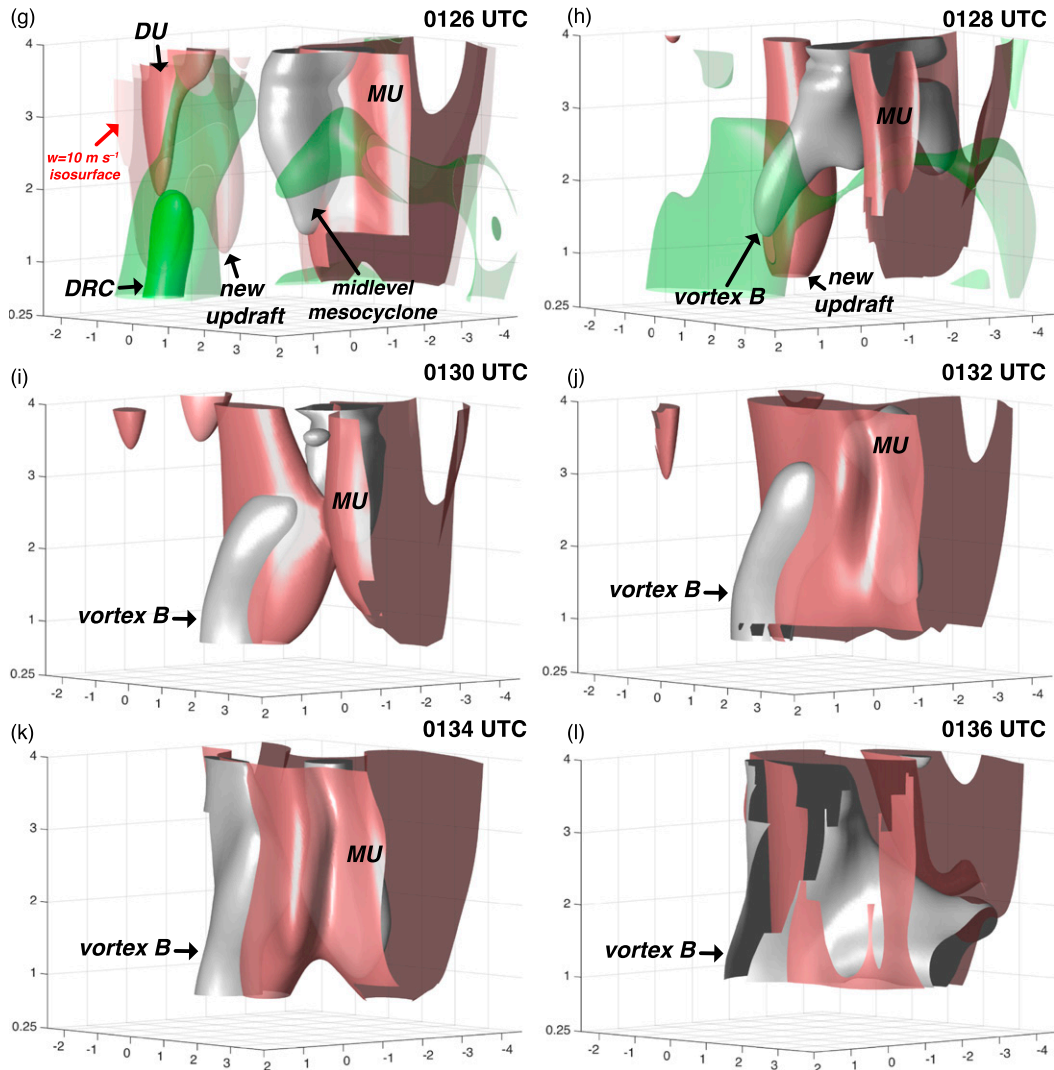


FIG. 9. (Continued)

momentum advection.) The HPGF field lines also are consistent with the observed southward shunting of vortex A in the 0124–0128 UTC period (Figs. 8e–g). As for why new updraft development took place on the northern flank of the DRC and not also on the southern flank, one plausible explanation is differences in low-level buoyancy ( $Dw/Dt$  is governed by both the VPPGF and buoyancy), with colder air being observed at the surface on the southern flank of the DRC than on its northern flank (Fig. 10c).

## 5. Discussion

The Clinton storm exemplifies the predictability challenges of tornadogenesis within supercell storms. The storm was in an environment extremely favorable for

supercell storms and tornadoes (STP as high as 4), yet was nontornadic or only marginally tornadic for the vast majority of its life, despite displaying supercell characteristics on radar for hours. On the scale of the low-level mesocyclone, the storm is similar to previous supercell storms. Vortex lines that emanate from the low-level mesocyclone either angle toward the midlevel mesocyclone or “arch” toward the southwestern flank of the cold pool (Fig. 9a); the latter vortex line characteristic has been interpreted as indicating a significant contribution to low-level mesocyclone rotation from baroclinic vorticity generation (Straka et al. 2007; Markowski et al. 2008, 2014; Markowski and Richardson 2014). Moreover, the amount of circulation associated with the low-level mesocyclone—even when nontornadic or marginally tornadic, at least within 1 km of

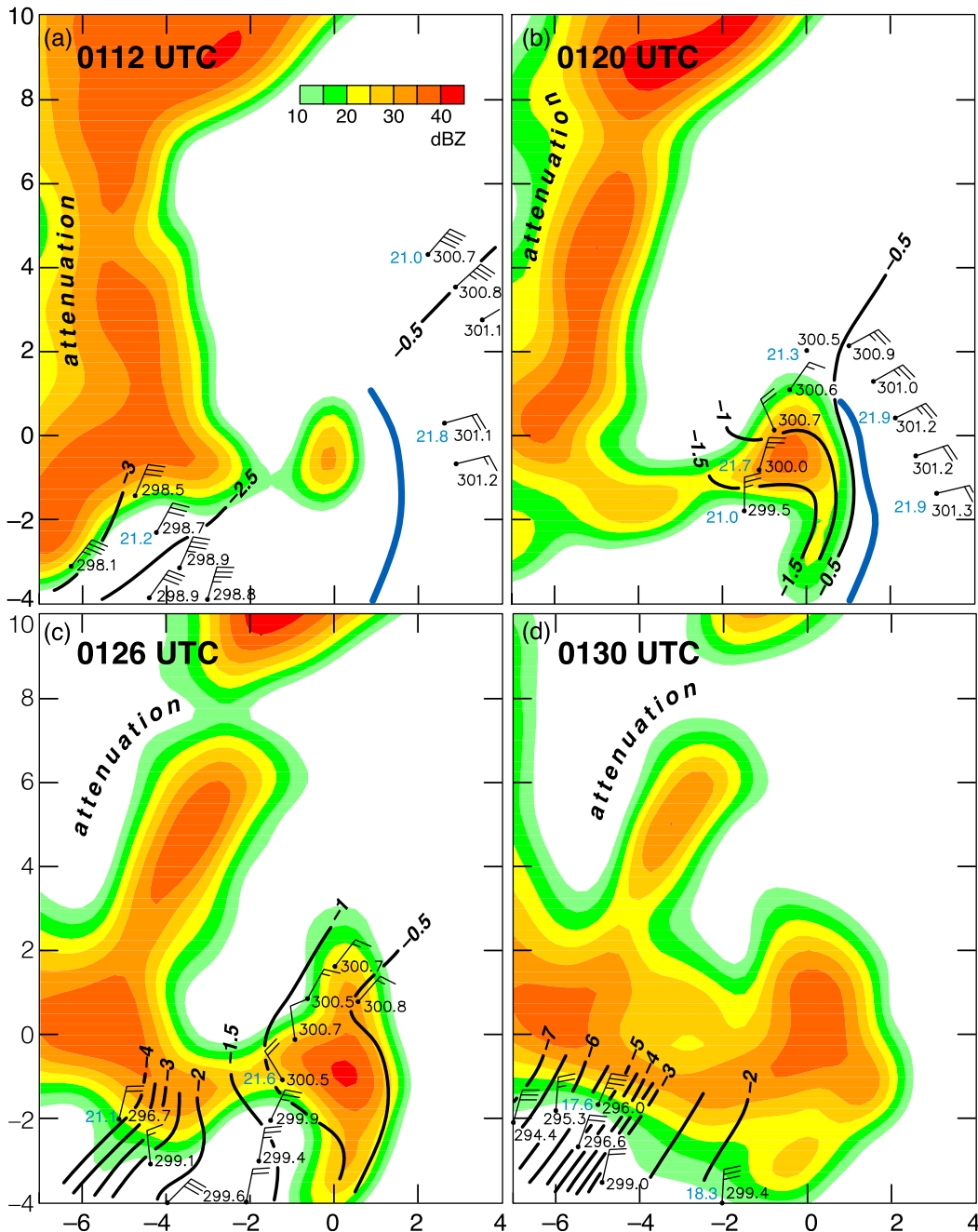


FIG. 10. Manual analyses of mobile mesonet observations of perturbation potential temperature ( $\theta'$ ; contours every 0.5 K), assuming an environmental potential temperature of 301.3 K, at (a) 0112, (b) 0120, (c) 0126, and (d) 0130 UTC. The time-space conversion used to create the analyses assumes a steady state for a period of  $\pm 300$  s centered on each analysis time. Station models depict storm-relative winds (half barb =  $2.5 \text{ m s}^{-1}$ ; full barb =  $5 \text{ m s}^{-1}$ ) and  $\theta$  values (black numerals). The objectively analyzed logarithmic reflectivity factor (dBZ) from the DOW7 radar at  $z = 0.75 \text{ km}$  is also displayed in each panel (color shading). The gust front locations derived from the dual-Doppler wind syntheses are indicated with heavy blue lines in (a) and (b). Wet-bulb potential temperatures  $\theta_w$  at select locations are also indicated (blue numerals); values are in  $^{\circ}\text{C}$  in order to facilitate comparison with Fig. 3a.

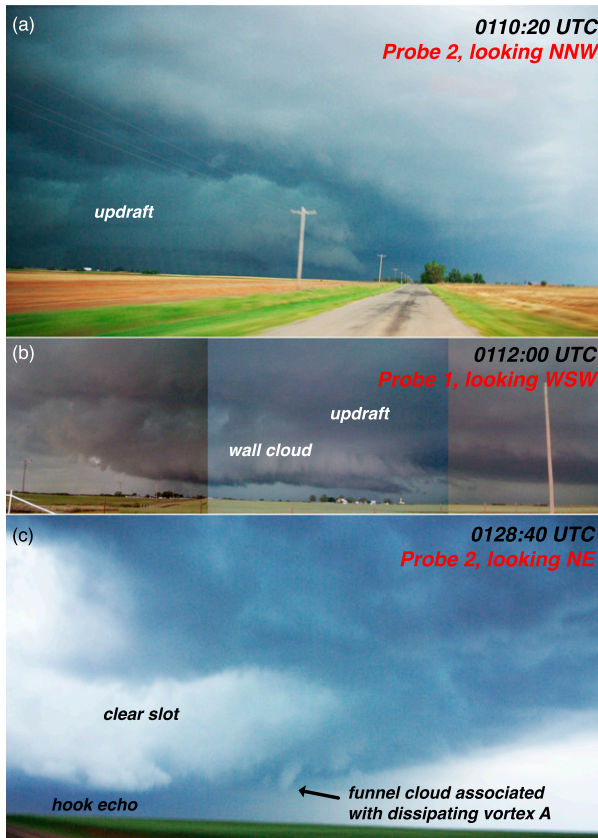


FIG. 11. Photographs of the 12 May 2010 storm at (a) 0110:20, (b) 0112:00, and (c) 0128:40 UTC. The contrast has been enhanced in (a) and (c), relative to the original photographs. The location from which the photograph in (a) was taken is shown in Fig. 4. The location from which the photograph in (b) was taken is shown in Figs. 4 and 8b. The location from which the photograph in (c) was taken is shown in Figs. 4, 5f, and 8g. The photographs in (a) and (c) were provided by J. Marquis and O. Shieh from the Probe 2 mobile mesonet vehicle. The photographs in (b) were taken by P. Markowski from the Probe 1 mobile mesonet vehicle.

the axis of rotation—is similar to the amount of circulation associated with supercells that produced strong tornadoes. Figure 15 compares  $C$  versus radius in the Clinton storm and in the Goshen County storm intercepted by VORTEX2, which produced an EF2 tornado only 4 min after the time shown in the figure. One must conclude that the Clinton storm had ample far-field circulation for producing a significant tornado all along, but that low-level convergence was lacking. Indeed, in the 0106–0126 UTC period, the updraft in the vicinity of  $\zeta_{\max}$  at low levels is somewhat weak and detached from the main updraft of the storm, as described in section 3.

Potential temperature deficits ( $<2$  K) and implied negative buoyancy within the circulation, in addition to  $\theta_w$  deficits ( $<1$  K), are all relatively small within the

limited time window sampled (Figs. 10b,c), at least relative to observations or simulations of tornadic storms (e.g., Markowski et al. 2002; Grzych et al. 2007; Hirth et al. 2008; Snook and Xue 2008; Markowski and Richardson 2014; Coffey and Parker 2017). Therefore, it would seem most likely that the Clinton storm's upward-directed VPPGF was inadequate during its nontornadic and marginally tornadic periods. The failure mode described here is exactly the failure mode in the Coffey and Parker (2017, 2018) and Coffey et al. (2017) simulation studies: there is ample surface vorticity, the outflow is not too cold, and the missing ingredient is a strong, steady, upward-directed VPPGF in the nontornadic storms.

As explained in section 4, the sudden appearance of the DRC was associated with rapid changes in the storm. A new updraft pulse formed on the flank of the DRC, which was closely followed by explosive growth of  $\zeta$  and  $C$ . Would the tornadogenesis associated with vortex B ever have occurred without the development of the DRC? Was the DRC itself a result of a reversal in the VPPGF (from upward to downward directed) in the vicinity of vortex A? Would vortex A eventually have developed into a significant tornado if the DRC had not formed (the DRC reversed the sign of  $\partial C/\partial t$ ; Fig. 13)? These questions are impossible to answer, unfortunately. It is hard to imagine how the complicated evolution of the Clinton storm in the  $\sim 0116$ – $0130$  UTC time period could have been anticipated. It also would have been impossible to detect with a WSR-88D, at least one situated more than  $\sim 25$  km away and completing volumes every 5 min [i.e., the case of the Clinton storm might have looked similar to the DRC-followed-by-tornado cases documented in WSR-88D data by Rasmussen et al. (2006) and Kennedy et al. (2007a,b)].

If it can be assumed that the DRC was not merely coincidental, its role in tornadogenesis in the Clinton storm might differ from the role of DRC in the VORTEX2 Goshen County storm. In the Goshen County storm, Lagrangian analyses of circulation about pre-DRC and post-DRC material circuits revealed that the DRC altered both the trajectories of the parcels composing the circuits (therefore the path of integration about which the baroclinic forcing,  $\oint B dz$ , was evaluated, where  $B$  is the buoyancy), as well as the buoyancy field itself (Markowski et al. 2012b), leading to a rapid increase in circulation after the arrival of the DRC at low levels, which was followed shortly thereafter by tornadogenesis. In the Clinton storm, however, the DRC's most likely role seems to be in promoting the rapid updraft intensification on the northern flank of the DRC. Unfortunately, as explained in section 3, trajectories

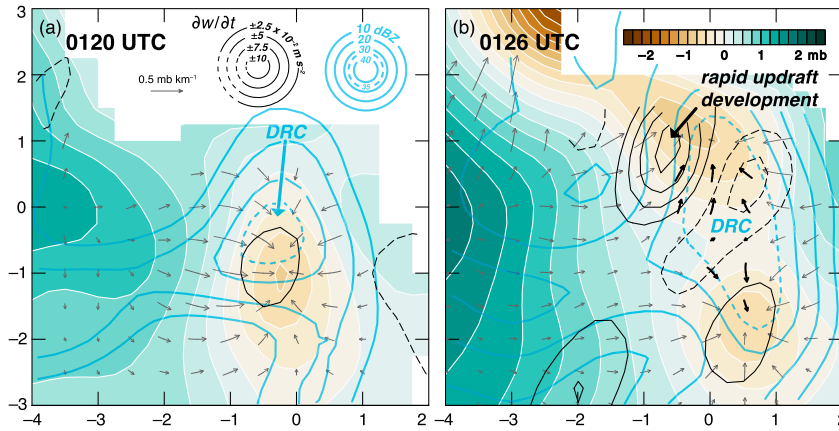


FIG. 12. Horizontal cross sections of perturbation pressure at  $z = 0.5$  km (color shading), local vertical velocity tendency at  $z = 0.75$  km [ $(\partial w/\partial t)$ ]; black contours of  $\pm 2.5, 5.0, 7.5,$  and  $10 \times 10^{-2} \text{ m s}^{-2}$ , negative contours dashed], and negative horizontal pressure gradient vectors at  $z = 0.5$  km (the vectors point toward lower pressure, in the direction of the horizontal pressure gradient force), obtained from the dual-Doppler wind syntheses, at (a) 0120 and (b) 0126 UTC. The objectively analyzed (uncalibrated) logarithmic reflectivity factor from DOW7 at  $z = 0.75$  km also is overlaid in each panel (light blue contours of 10, 20, 30, 35, and 40 dBZ; the intermediate 35-dBZ contour is dashed). In (b), the emboldened vectors indicate the direction of the pressure gradient force on the flanks of the DRC (see text for details).

could not be computed a meaningful distance backward in time owing to a large swath of missing velocities northeast of the Clinton storm’s low-level mesocyclone. Thus, a similar Lagrangian circulation analysis, which can reveal the importance of baroclinity, was precluded. The Eulerian circulation analysis presented in Fig. 13 merely shows that circulation about a fixed (1-km radius) ring increased as horizontal vorticity was tilted into the vertical within the ring beneath the intensifying updraft ( $\omega$ -flux term), and existing vertical vorticity from beyond the ring was fluxed into the ring by enhanced radial inflow beneath the intensifying updraft ( $\zeta$ -flux term). We cannot say how much of the vorticity appearing in either forcing might have been influenced by baroclinity prior to becoming vertical vorticity within the control rings.

Last, some comparisons to a recent high-resolution tornadic supercell simulation by Orf et al. (2017) are made, specifically, the prominent streamwise vorticity current (SVC) identified in their simulation. The authors defined the SVC as “a persistent ‘tube’ of streamwise vorticity located along the [forward-flank downdraft boundary] FFDB that flows rearward along the FFDB and eventually upward into the updraft. It is confined to a region immediately on the cool side of the FFDB where streamwise horizontal vorticity can be generated through baroclinic effects (p. 53).” Orf et al. found that the intensification of the low-level updraft prior to tornadogenesis occurred approximately simultaneously with the intensification of the SVC, tornadogenesis occurred very

near where the SVC was tilted upward by the main storm updraft (though the SVC did not feed the tornado directly), and tornado demise occurred “in conjunction with a dramatic weakening in the SVC.”

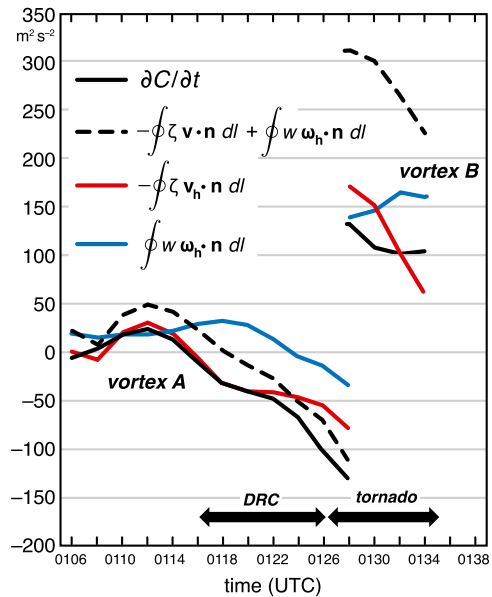


FIG. 13. Forcings for circulation at  $z = 0.75$  km about a 1-km-radius ring centered on  $\zeta_{\max}$ . The  $\zeta$ -flux and  $\omega$ -flux terms are indicated with red and blue lines, respectively, for both vortex A and vortex B. The sum of the forcings is indicated with a black dashed line, and the independently diagnosed circulation tendency ( $\partial C/\partial t$ ) is indicated with a solid black line. The time period of the tornado is based on the official record in *Storm Data*.

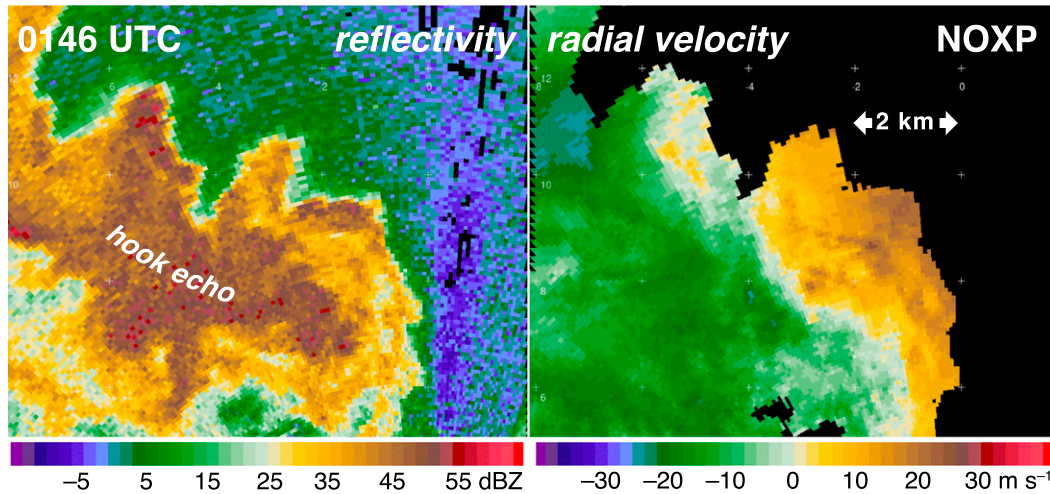


FIG. 14. Logarithmic reflectivity factor (dBZ) and radial velocity ( $\text{m s}^{-1}$ ) observed by NOXP ( $1.0^\circ$  elevation angle) at 0146 UTC in the hook echo region of the Clinton storm.

Figure 16 presents streamwise vorticity fields in the 0112–0132 UTC period, in which hints of a feature resembling Orf et al.’s SVC are occasionally visible. The feature—a  $\sim 1\text{--}2\text{-km}$ -wide band of enhanced streamwise vorticity extending northward from the low-level mesocyclone region—is poorly sampled, in that it is along the eastern edge of the region of usable velocity data and the data horizon is  $0.5\text{--}0.75\text{ km}$  AGL in this region. Setting these caveats aside, the band of enhanced streamwise vorticity intensifies during the time period leading up to

tornadogenesis, though cause-and-effect cannot be assigned, as also noted by Orf et al. An intensification of streamwise vorticity via horizontal stretching would be expected as air accelerates toward a rapidly intensifying low-level updraft.

### 6. Summary and conclusions

The 12 May 2010 supercell thunderstorm intercepted by VORTEX2, also known as the Clinton storm, produced an EF1 tornado near the end of an intensive observing period that included 32 min of dual-Doppler observations from a pair of DOW radars. The evolution detailed in sections 3 and 4 is summarized in Fig. 17. In roughly the first 20 min of observation (0106–0126 UTC 13 May), the storm possessed a strong low-level mesocyclone (vortex A) with a radial velocity differential of  $30\text{--}40\text{ m s}^{-1}$ , which was regarded as marginally tornadic (Figs. 17a–c). At 0116 UTC, a DRC was observed at an altitude of approximately 3 km, and in the ensuing 6 min, the DRC reached the surface (Fig. 17b). The low-level mesocyclone weakened rapidly after 0125 UTC, becoming unidentifiable by 0129 UTC. However, on the northern flank of the DRC, an updraft “pulse” was detected at 0126 UTC in the three-dimensional wind syntheses (Fig. 17c). A new, distinct low-level mesocyclone (vortex B) rapidly developed in conjunction with the intensifying updraft, and within the ensuing minute, a tornado was reported on the south side of Clinton (Fig. 17d). The Clinton storm case illustrates the challenges in predicting tornadogenesis within supercell storms even in environments known to be highly favorable for tornadoes.

We have high confidence in the following conclusions:

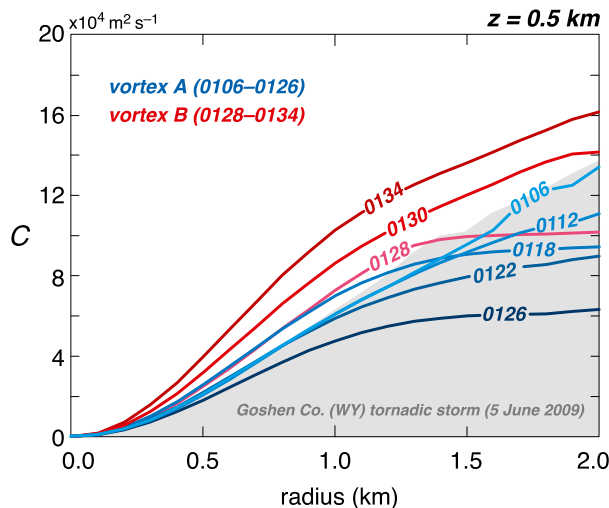


FIG. 15. Radial profiles of circulation about  $\zeta_{\text{max}}$  at  $z = 0.5\text{ km}$  at select times during the dual-Doppler data collection period. Profiles for vortex A (vortex B) are shades of blue (red). The radial profile of circulation in the Goshen County (WY) tornadic supercell intercepted by VORTEX2, 4 min prior to tornadogenesis, is underlaid for comparison [gray shading; see Fig. 19 of Markowski et al. (2012a)].

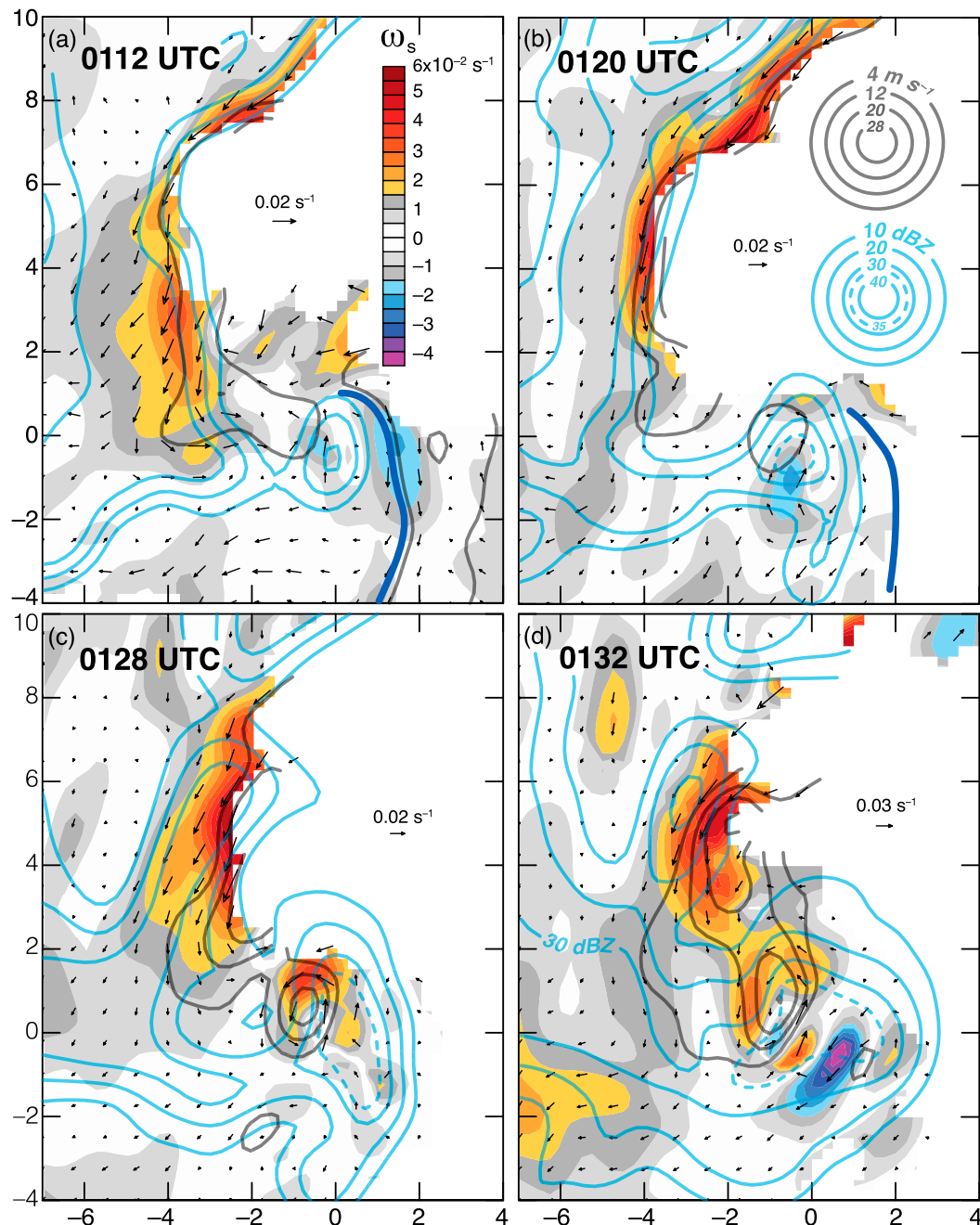


FIG. 16. Horizontal cross sections of streamwise vorticity ( $\omega_s$ , color shading), vertical velocity (dark gray contours every  $8 \text{ m s}^{-1}$  starting at  $4 \text{ m s}^{-1}$ ), and horizontal vorticity vectors (every third grid point) at  $z = 0.75 \text{ km}$  obtained from the dual-Doppler wind syntheses at (a) 0112, (b) 0120, (c) 0128, and (d) 0132 UTC. The objectively analyzed (uncalibrated) logarithmic reflectivity factor from DOW7 also is overlaid in each panel (light blue contours of 10, 20, 30, 35, and 40 dBZ; the intermediate 35-dBZ contour is dashed). Gust front locations are indicated with the heavy blue line in (a) and (b).

- Even when vortex A was only marginally tornadic, it possessed sufficient circulation to produce a significant tornado;
- The sudden formation and intensification of vortex B, ultimately leading to tornadogenesis, occurred in

conjunction with the development of an updraft pulse on the northern flank of the DRC;

- The air mass toward the tip of the hook echo, in the vicinity of vortex A and vortex B, was characterized by relatively small  $\theta$  and  $\theta_w$  deficits ( $<2$  and  $<1 \text{ K}$ ,

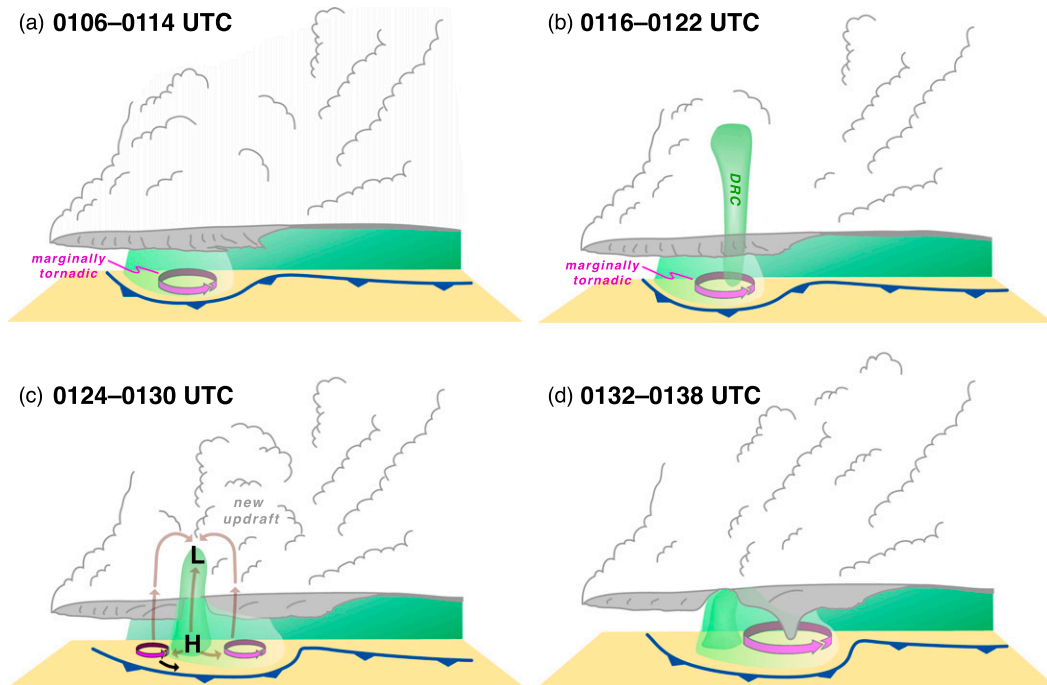


FIG. 17. Schematic summarizing the evolution of the Clinton storm: (a) 0106–0114, (b) 0116–0122, (c) 0124–0130, and (d) 0132–0138 UTC. Curved magenta arrows encircle cyclonic vorticity maxima, with the size of the arrows being proportional to vorticity magnitude. Some plausible perturbation pressure gradient force field lines in the vicinity of the DRC are shown in (c). The black arrow in (c) indicates the storm-relative motion of the cyclonic vortex as it weakens.

respectively), comparable to what has been observed in supercells that produce significant tornadoes (total buoyancy could not be diagnosed, however).

The following conclusions are more tentative:

- Vortex A remained, at best, only marginally tornadic, despite being associated with relatively large circulation, owing to an insufficiently strong low-level updraft;
- The sudden demise of vortex A was brought about by the DRC (the low-level mesocyclone developed radial outflow once the DRC reached low levels in close proximity to vortex A);
- The sudden formation of an updraft pulse, and the accompanying formation and rapid intensification of vortex B, were brought about by the DRC.

Although there are some tornado outbreak days on which nearly all storms are tornadic, the vast majority of tornado outbreaks feature nontornadic storms that coexist near tornadic storms. Even the tornadic storms, on outbreak days and on days when the severe weather threat is more isolated, are rarely tornadic for more than a small fraction of their total lifetime. This is even frequently the case for storms occurring in environments favorable for tornadoes throughout the life of the storm. Additional research is needed on

the subject of tornadogenesis “triggers”; that is, developments either internal or external to the storm that can suddenly and quickly transform a nontornadic supercell into a tornadic one (or influence a tornado after a tornado has formed). Such triggers occasionally seem to take the form of DRCs, but in other cases, so-called internal outflow surges (Lee et al. 2004; Finley and Lee 2004) also appear to be capable of instigating tornadogenesis (e.g., Marquis et al. 2008; Mashiko et al. 2009; Wurman et al. 2010; Kosiba et al. 2013; Schenkman et al. 2014, 2016). A treasure trove of VORTEX2 datasets remain to be analyzed. The datasets may offer some clues.

*Acknowledgments.* We thank the countless VORTEX2 PIs, students, and other participants, without which the project would not have been possible. We are grateful for the generous support of VORTEX2 from the National Science Foundation (NSF) and the National Oceanic and Atmospheric Administration. The data collection and analysis were supported by NSF Awards ATM-0801035, AGS-1157646, and AGS-1536460. We are especially thankful for the assistance of Josh Wurman, Karen Kosiba, and Paul Robinson in collecting and analyzing the DOW data.

The DOW radars are NSF Lower Atmospheric Observing Facilities. Don Burgess graciously provided NOXP radar data. Radar data were edited using the SOLO3 software provided by the Earth Observing Laboratory at the National Center for Atmospheric Research (NCAR). Radar data were objectively analyzed using software originally written by David Dowell. The photographs in Figs. 11a and 11c were provided by Owen Shieh and Jim Marquis. We also thank Skip Talbot for providing video of the storm. Last, we appreciate the selfless donation of time and constructive critiques provided by the reviewers (Johannes Dahl, Matt Parker, and one anonymous reviewer).

## REFERENCES

- Alexander, C., and J. Wurman, 2008: Updated mobile radar climatology of supercell tornado structures and dynamics. *24th Conf. on Severe Local Storms*, Savannah, GA, Amer. Meteor. Soc., 19.4, [https://ams.confex.com/ams/24SLS/techprogram/paper\\_141821.htm](https://ams.confex.com/ams/24SLS/techprogram/paper_141821.htm).
- Anderson-Frey, A. K., Y. P. Richardson, A. R. Dean, R. L. Thompson, and B. T. Smith, 2016: Investigation of near-storm environments for tornado events and warnings. *Wea. Forecasting*, **31**, 1771–1790, <https://doi.org/10.1175/WAF-D-16-0046.1>.
- Barnes, S. L., 1964: A technique for maximizing details in numerical weather map analysis. *J. Appl. Meteor.*, **3**, 396–409, [https://doi.org/10.1175/1520-0450\(1964\)003<0396:ATFMDI>2.0.CO;2](https://doi.org/10.1175/1520-0450(1964)003<0396:ATFMDI>2.0.CO;2).
- Beck, J. R., J. L. Schroeder, and J. M. Wurman, 2006: High-resolution, dual-Doppler analyses of the 29 May 2001 Kress, Texas, cyclic supercell. *Mon. Wea. Rev.*, **134**, 3125–3148, <https://doi.org/10.1175/MWR3246.1>.
- Bluestein, H. B., and A. L. Pazmany, 2000: Observations of tornadoes and other convective phenomena with a mobile, 3-mm wavelength, Doppler radar: The spring 1999 field experiment. *Bull. Amer. Meteor. Soc.*, **81**, 2939–2952, [https://doi.org/10.1175/1520-0477\(2000\)081<2939:OOTAO>2.3.CO;2](https://doi.org/10.1175/1520-0477(2000)081<2939:OOTAO>2.3.CO;2).
- Byko, Z., P. Markowski, Y. Richardson, J. Wurman, and E. Adelman, 2009: Descending reflectivity cores in supercell thunderstorms observed by mobile radars and in a high-resolution numerical simulation. *Wea. Forecasting*, **24**, 155–186, <https://doi.org/10.1175/2008WAF2222116.1>.
- Coffer, B. E., and M. D. Parker, 2015: Impacts of increasing low-level shear on supercells during the early evening transition. *Mon. Wea. Rev.*, **143**, 1945–1969, <https://doi.org/10.1175/MWR-D-14-00328.1>.
- , and —, 2017: Simulated supercells in nontornadoic and tornadoic VORTEX2 environments. *Mon. Wea. Rev.*, **145**, 149–180, <https://doi.org/10.1175/MWR-D-16-0226.1>.
- , and —, 2018: Is there a “tipping point” between simulated nontornadoic and tornadoic supercells in VORTEX2 environments? *Mon. Wea. Rev.*, **146**, 2667–2693, <https://doi.org/10.1175/MWR-D-18-0050.1>.
- , —, J. M. Dahl, L. J. Wicker, and A. J. Clark, 2017: Volatility of tornadogenesis: An ensemble of simulated nontornadoic and tornadoic supercells in VORTEX2 environments. *Mon. Wea. Rev.*, **145**, 4605–4625, <https://doi.org/10.1175/MWR-D-17-0152.1>.
- Davies-Jones, R., 2015: A review of supercell and tornado dynamics. *Atmos. Res.*, **158–159**, 274–291, <https://doi.org/10.1016/j.atmosres.2014.04.007>.
- , R. J. Trapp, and H. B. Bluestein, 2001: Tornadoes and tornadoic storms. *Severe Convective Storms*, Meteor. Monogr., No. 50, 167–221, <https://doi.org/10.1175/0065-9401-28.50.167>.
- Emanuel, K. A., 1994: *Atmospheric Convection*. Oxford University Press, 580 pp.
- Finley, C. A., and B. D. Lee, 2004: High resolution mobile mesonet observations of RFD surges in the June 9 Basset, Nebraska supercell during Project ANSWERS 2003. *22nd Conf. on Severe Local Storms*, Hyannis, MA, Amer. Meteor. Soc., P11.3, <http://ams.confex.com/ams/pdfpapers/82005.pdf>.
- Gal-Chen, T., 1978: A method for the initialization of the anelastic equations: Implications for matching models with observations. *Mon. Wea. Rev.*, **106**, 587–606, [https://doi.org/10.1175/1520-0493\(1978\)106<0587:AMFTIO>2.0.CO;2](https://doi.org/10.1175/1520-0493(1978)106<0587:AMFTIO>2.0.CO;2).
- Grzych, M. L., B. D. Lee, and C. A. Finley, 2007: Thermodynamic analysis of supercell rear-flank downdrafts from Project ANSWERS. *Mon. Wea. Rev.*, **135**, 240–246, <https://doi.org/10.1175/MWR3288.1>.
- Hane, C. E., and P. S. Ray, 1985: Pressure and buoyancy fields derived from Doppler radar data in a tornadoic thunderstorm. *J. Atmos. Sci.*, **42**, 18–35, [https://doi.org/10.1175/1520-0469\(1985\)042<0018:PABFDF>2.0.CO;2](https://doi.org/10.1175/1520-0469(1985)042<0018:PABFDF>2.0.CO;2).
- Hirth, B. D., J. L. Schroeder, and C. C. Weiss, 2008: Surface analysis of the rear-flank downdraft outflow in two tornadoic supercells. *Mon. Wea. Rev.*, **136**, 2344–2363, <https://doi.org/10.1175/2007MWR2285.1>.
- Houze, R. A., Jr., 1993: *Cloud Dynamics*. Academic Press, 573 pp.
- Kennedy, A. D., J. M. Straka, and E. N. Rasmussen, 2007a: A statistical study of the association of DRCs with supercells and tornadoes. *Wea. Forecasting*, **22**, 1191–1199, <https://doi.org/10.1175/2007WAF2006095.1>.
- , —, and —, 2007b: A visual observation of the 6 June 2005 descending reflectivity core. *Electron. J. Severe Storms Meteor.*, **2** (6), <http://www.ejssm.org/ojs/index.php/ejssm/article/viewArticle/16>.
- Koch, S. E., M. DesJardins, and P. J. Kocin, 1983: An interactive Barnes objective map analysis scheme for use with satellite and conventional data. *J. Climate Appl. Meteor.*, **22**, 1487–1503, [https://doi.org/10.1175/1520-0450\(1983\)022<1487:AIBOMA>2.0.CO;2](https://doi.org/10.1175/1520-0450(1983)022<1487:AIBOMA>2.0.CO;2).
- Kosiba, K., J. Wurman, Y. Richardson, P. Markowski, P. Robinson, and J. Marquis, 2013: Genesis of the Goshen County, Wyoming, tornado (5 June 2009). *Mon. Wea. Rev.*, **141**, 1157–1181, <https://doi.org/10.1175/MWR-D-12-00056.1>.
- Lee, B. D., C. A. Finley, and P. Skinner, 2004: Thermodynamic and kinematic analysis of multiple RFD surges for the 24 June 2003 Manchester, SD cyclic tornadoic supercell during Project ANSWERS 2003. *22nd Conf. on Severe Local Storms*, Hyannis, MA, Amer. Meteor. Soc., P11.2, [https://ams.confex.com/ams/11aram22sls/techprogram/paper\\_82000.htm](https://ams.confex.com/ams/11aram22sls/techprogram/paper_82000.htm).
- Maddox, R. A., 1993: Diurnal low-level wind oscillation and storm-relative helicity. *The Tornado: Its Structure, Dynamics, Prediction, and Hazards*, Geophys. Monogr., Vol. 79, Amer. Geophys. Union, 591–598.
- Majcen, M., P. Markowski, Y. Richardson, D. Dowell, and J. Wurman, 2008: Multi-pass objective analyses of radar data. *J. Atmos. Oceanic Technol.*, **25**, 1845–1858, <https://doi.org/10.1175/2008JTECHA1089.1>.
- Markowski, P. M., and Y. P. Richardson, 2009: Tornadogenesis: Our current understanding, forecasting considerations, and

- questions to guide future research. *Atmos. Res.*, **93**, 3–10, <https://doi.org/10.1016/j.atmosres.2008.09.015>.
- , and —, 2014: The influence of environmental low-level shear and cold pools on tornadogenesis: Insights from idealized simulations. *J. Atmos. Sci.*, **71**, 243–275, <https://doi.org/10.1175/JAS-D-13-0159.1>.
- , J. M. Straka, and E. N. Rasmussen, 2002: Direct surface thermodynamic observations within the rear-flank downdrafts of nontornadic and tornadic supercells. *Mon. Wea. Rev.*, **130**, 1692–1721, [https://doi.org/10.1175/1520-0493\(2002\)130<1692:DSTOWT>2.0.CO;2](https://doi.org/10.1175/1520-0493(2002)130<1692:DSTOWT>2.0.CO;2).
- , C. Hannon, J. Frame, E. Lancaster, A. Pietrycha, R. Edwards, and R. Thompson, 2003: Characteristics of vertical wind profiles near supercells obtained from the Rapid Update Cycle. *Wea. Forecasting*, **18**, 1262–1272, [https://doi.org/10.1175/1520-0434\(2003\)018<1262:COVWPN>2.0.CO;2](https://doi.org/10.1175/1520-0434(2003)018<1262:COVWPN>2.0.CO;2).
- , J. M. Straka, E. N. Rasmussen, R. P. Davies-Jones, Y. Richardson, and J. Trapp, 2008: Vortex lines within low-level mesocyclones obtained from pseudo-dual-Doppler radar observations. *Mon. Wea. Rev.*, **136**, 3513–3535, <https://doi.org/10.1175/2008MWR2315.1>.
- , and Coauthors, 2012a: The pretornadic phase of the Goshen County, Wyoming, supercell of 5 June 2009 intercepted by VORTEX2. Part I: Evolution of kinematic and surface thermodynamic fields. *Mon. Wea. Rev.*, **140**, 2887–2915, <https://doi.org/10.1175/MWR-D-11-00336.1>.
- , and Coauthors, 2012b: The pretornadic phase of the Goshen County, Wyoming, supercell of 5 June 2009 intercepted by VORTEX2. Part II: Intensification of low-level rotation. *Mon. Wea. Rev.*, **140**, 2916–2938, <https://doi.org/10.1175/MWR-D-11-00337.1>.
- , Y. P. Richardson, and G. H. Bryan, 2014: The origins of vortex sheets in a simulated supercell thunderstorm. *Mon. Wea. Rev.*, **142**, 3944–3954, <https://doi.org/10.1175/MWR-D-14-00162.1>.
- Marquis, J. N., Y. P. Richardson, J. M. Wurman, and P. M. Markowski, 2008: Single- and dual-Doppler analysis of a tornadic vortex and surrounding storm scale flow in the Crowell, Texas, supercell of 30 April 2000. *Mon. Wea. Rev.*, **136**, 5017–5043, <https://doi.org/10.1175/2008MWR2442.1>.
- , —, P. Markowski, D. Dowell, and J. Wurman, 2012: Tornado maintenance investigated with high-resolution dual-Doppler and EnKF analysis. *Mon. Wea. Rev.*, **140**, 3–27, <https://doi.org/10.1175/MWR-D-11-00025.1>.
- Mashiko, W., H. Niino, and T. Kato, 2009: Numerical simulation of tornadogenesis in an outer-rainband minisupercell of Typhoon Shanshan on 17 September 2006. *Mon. Wea. Rev.*, **137**, 4238–4260, <https://doi.org/10.1175/2009MWR2959.1>.
- Mead, C. M., and R. L. Thompson, 2011: Environmental characteristics associated with nocturnal significant-tornado events in the Great Plains. *Electron. J. Severe Storms Meteor.*, **6** (6), <http://www.ejssm.org/ojs/index.php/ejssm/article/viewArticle/84>.
- Melnikov, V., D. Zrnčić, A. Ryzhkov, A. Zahrai, and J. Carter, 2009: Validation of attenuation correction at X band performed with collocated S-band polarimetric radar. *34th Conf. on Radar Meteorology*, Williamsburg, VA, Amer. Meteor. Soc., 11A.5, <https://ams.confex.com/ams/pdfpapers/155322.pdf>.
- Orf, L., R. Wilhelmsen, B. Lee, C. Finley, and A. Houston, 2017: Evolution of a long-track violent tornado within a simulated supercell. *Bull. Amer. Meteor. Soc.*, **98**, 45–68, <https://doi.org/10.1175/BAMS-D-15-00073.1>.
- Palmer, R. D., and Coauthors, 2009: Weather radar education at the University of Oklahoma—An integrated interdisciplinary approach. *Bull. Amer. Meteor. Soc.*, **90**, 1277–1282, <https://doi.org/10.1175/2009BAMS2738.1>.
- Rasmussen, E. N., J. M. Straka, M. S. Gilmore, and R. Davies-Jones, 2006: A preliminary survey of rear-flank descending reflectivity cores in supercell storms. *Wea. Forecasting*, **21**, 923–938, <https://doi.org/10.1175/WAF962.1>.
- Schenkman, A. D., M. Xue, and M. Hu, 2014: Tornadogenesis in a high-resolution simulation of the 8 May 2003 Oklahoma City supercell. *J. Atmos. Sci.*, **71**, 130–154, <https://doi.org/10.1175/JAS-D-13-073.1>.
- , —, and D. T. Dawson II, 2016: The cause of internal outflow surges in a high-resolution simulation of the 8 May 2003 Oklahoma City tornadic supercell. *J. Atmos. Sci.*, **73**, 353–370, <https://doi.org/10.1175/JAS-D-15-0112.1>.
- Shabbott, C. J., and P. M. Markowski, 2006: Surface in situ observations within the outflow of forward-flank downdrafts of supercell thunderstorms. *Mon. Wea. Rev.*, **134**, 1422–1441, <https://doi.org/10.1175/MWR3131.1>.
- Snook, N., and M. Xue, 2008: Effects of microphysical drop size distribution on tornadogenesis in supercell thunderstorms. *Geophys. Res. Lett.*, **35**, L24803, <https://doi.org/10.1029/2008GL035866>.
- Straka, J. M., E. N. Rasmussen, and S. E. Fredrickson, 1996: A mobile mesonet for finescale meteorological observations. *J. Atmos. Oceanic Technol.*, **13**, 921–936, [https://doi.org/10.1175/1520-0426\(1996\)013<0921:AMMFFM>2.0.CO;2](https://doi.org/10.1175/1520-0426(1996)013<0921:AMMFFM>2.0.CO;2).
- , —, R. P. Davies-Jones, and P. M. Markowski, 2007: An observational and idealized numerical examination of low-level counter-rotating vortices toward the rear flank of supercells. *Electron. J. Severe Storms Meteor.*, **2** (8), <http://www.ejssm.org/ojs/index.php/ejssm/article/viewArticle/32>.
- Thompson, R. L., R. Edwards, J. A. Hart, K. L. Elmore, and P. M. Markowski, 2003: Close proximity soundings within supercell environments obtained from the Rapid Update Cycle. *Wea. Forecasting*, **18**, 1243–1261, [https://doi.org/10.1175/1520-0434\(2003\)018<1243:CPWSE>2.0.CO;2](https://doi.org/10.1175/1520-0434(2003)018<1243:CPWSE>2.0.CO;2).
- , B. T. Smith, J. S. Grams, A. R. Dean, and C. Broyles, 2012: Convective modes for significant severe thunderstorms in the contiguous United States. Part II: Supercell and QLCS tornado environments. *Wea. Forecasting*, **27**, 1136–1154, <https://doi.org/10.1175/WAF-D-11-00116.1>.
- Trapp, R. J., and M. L. Weisman, 2003: Low-level mesovortices within squall lines and bow echoes. Part II: Their genesis and implications. *Mon. Wea. Rev.*, **131**, 2804–2823, [https://doi.org/10.1175/1520-0493\(2003\)131<2804:LMWSLA>2.0.CO;2](https://doi.org/10.1175/1520-0493(2003)131<2804:LMWSLA>2.0.CO;2).
- Waugh, S., and S. E. Fredrickson, 2010: An improved aspirated temperature system for mobile meteorological observations, especially in severe weather. *25th Conf. on Severe Local Storms*, Denver, CO, Amer. Meteor. Soc., P5.2, [https://ams.confex.com/ams/25SLS/techprogram/paper\\_176205.htm](https://ams.confex.com/ams/25SLS/techprogram/paper_176205.htm).
- Wurman, J., 2001: The DOW mobile multiple-Doppler network. Preprints, *30th Int. Conf. on Radar Meteorology*, Munich, Germany, Amer. Meteor. Soc., P3.3, [https://ams.confex.com/ams/30radar/techprogram/paper\\_21572.htm](https://ams.confex.com/ams/30radar/techprogram/paper_21572.htm).
- , J. M. Straka, and E. N. Rasmussen, 1996: Fine-scale Doppler radar observations of tornadoes. *Science*, **272**, 1774–1777, <https://doi.org/10.1126/science.272.5269.1774>.
- , J. Straka, E. Rasmussen, M. Randall, and A. Zahrai, 1997: Design and deployment of a portable, pencil-beam, pulsed, 3-cm Doppler radar. *J. Atmos. Oceanic Technol.*, **14**, 1502–1512, [https://doi.org/10.1175/1520-0426\(1997\)014<1502:DADOAP>2.0.CO;2](https://doi.org/10.1175/1520-0426(1997)014<1502:DADOAP>2.0.CO;2).
- , Y. Richardson, C. Alexander, S. Weygant, and P. F. Zhang, 2007a: Dual-Doppler analysis of winds and vorticity budget

- terms near a tornado. *Mon. Wea. Rev.*, **135**, 2392–2405, <https://doi.org/10.1175/MWR3404.1>.
- , —, —, —, and —, 2007b: Dual-Doppler and single-Doppler analysis of a tornadic storm undergoing mergers and repeated tornadogenesis. *Mon. Wea. Rev.*, **135**, 736–758, <https://doi.org/10.1175/MWR3276.1>.
- , K. A. Kosiba, P. Markowski, Y. Richardson, D. Dowell, and P. Robinson, 2010: Finescale and dual-Doppler analysis of tornado intensification, maintenance, and dissipation in the Orleans, Nebraska, tornadic supercell. *Mon. Wea. Rev.*, **138**, 4439–4455, <https://doi.org/10.1175/2010MWR3330.1>.
- , D. Dowell, Y. Richardson, P. Markowski, E. Rasmussen, D. Burgess, L. Wicker, and H. Bluestein, 2012: Verification of the Origins of Rotation in Tornadoes Experiment 2: VORTEX2. *Bull. Amer. Meteor. Soc.*, **93**, 1147–1170, <https://doi.org/10.1175/BAMS-D-11-00010.1>.